Cross-field potential hill arisen eccentrically in toroidal electron cyclotron resonance plasmas in the Low Aspect ratio Torus Experiment device to regulate electron and ion flows from source to boundary

AUTHOR(S):

Kuroda, Kengoh; Wada, Manato; Uchida, Masaki; Tanaka, Hitoshi; Maekawa, Takashi

Cross-field potential hill arisen eccentrically in toroidal ECR plasmas in the LATE device to regulate electron and ion flows from source to boundary

Kengoh Kuroda, Manato Wada, Masaki Uchida, Hitoshi Tanaka and Takashi Maekawa

Graduate School of Energy Science, Kyoto University, Kyoto 606-8502, Japan

E-mail: kuroda.kengoh.65r@st.kyoto-u.ac.jp

Abstract.

We have investigated the electron and ion flows in toroidal electron cyclotron resonance (ECR) plasmas maintained by a 2.45 GHz microwave power around 1 kW under a simple toroidal field in the low aspect ratio torus experiment (LATE) device. We have found that a vertically uniform ridge of electron pressure that also constitutes the source belt of electron impact ionization is formed along just lower field side of the ECR layer and a cross-field potential hill ($V_S \cong$30 V while $T_e \cong$10 eV), eccentrically shifted toward the corner formed by the top panel and the ECR layer, arises. Combination of the hill-driven $E \times B$ drift and the vertical drift due to the field gradient and curvature, being referred to as vacuum toroidal field (VTF) drift, realizes steady flows of electrons and ions from the source to the boundary. In particular, the ions, of which VTF drift velocity is much slower than the electron VTF drift velocity near the source belt, are carried by the $E \times B$ drift around the hill to the vicinity of the top panel, where the ion VTF drift is enhanced on the steep down slope of potential toward the top panel. On the other hand the electron temperature strongly decreases in this area. Thus the carrier of VTF drift current is replaced from the electrons to the ions before the top panel, enabling the current circulation through the top and bottom panels and the vessel (electrons mainly to the bottom and ions mainly to the top) that keeps the charge neutrality very high. A few percent of electrons from the source turn around the hill by 360 degree and reentry the source belt from the high field side as seed electrons for the impact ionization, keeping the discharge stable.

1. Introduction

There has been considerable interest in electron cyclotron resonance (ECR) heated plasmas in a toroidal field with no rotational transform. By injection of microwaves at the ECR frequency, breakdown takes place at the ECR layer and the discharge is maintained by the deposition of the microwave power at the ECR layer and/or the upper hybrid resonance (UHR) layer [1, 2]. This is a standard method of pre-ionization and heating to assist the start-up of plasma current in tokamaks [3]. The ECR plasmas also served as a target plasma for solenoid-free start-up of tokamaks by lower hybrid waves [4, 5] and their characteristics was investigated in connection with confinement and equilibrium in the open field configuration [6, 7]. In addition to the usage for tokamak startup, ECR-heated plasmas in small toroidal devices, which are often produced by 2.45 GHz microwave power at a power level of 1 kW, have been frequently used as a bed of various basic studies in plasma physics. In the TORPEX device particle confinement [8], charged particle generation [9], blob generation [10] were investigated. In the Helimak device drift wave instability was studied [11]. In the Blaaman device particle transport by turbulence was studied [12]. In the CDX device [13, 14] and in the Low Aspect ratio Torus Experiment (LATE) device [15, 16] it was found that a toroidal current was generated when a weak vertical field was superposed.

Suppose an axisymmetric toroidal plasma immersed in a toroidal magnetic field B_ϕ in the cylindrical coordinate (R, ϕ, Z) system with Z-axis being the symmetric axis of the torus, each charged particle drifts vertically across the field lines due to the radial gradient and curvature of B_ϕ with the velocity given by

$$V_{VTF} = \frac{m(v_\parallel^2 + v_\perp^2/2)}{qB_\phi R} \tag{1}$$

Here, B_ϕ is the toroidal field at the radial coordinate R; q and m is the charge and mass ; and $\parallel$ and $\perp$ denotes the parallel and perpendicular components of the velocity to the field, respectively. Hereafter, this vertical drift is referred to as vacuum-toroidal-field (VTF) drift since the toroidal field in these ECR-heated plasmas is essentially vacuum field with negligibly small paramagnetic and diamagnetic effects ($\beta \simeq 0.01\%$ in the present experiment). The local current density by electron (ion) VTF-drift is given by summing up the VTF-drift current of every electron (ion) over the Maxwellian velocity distribution and is written in terms of the local pressure $p_e(p_i)$;

$$j_{VTFe(i)} = \frac{2p_{e(i)}}{RB_\phi} \tag{2}$$

Equation (1) predicts that the electrons drift downwards while the positive ions drift upwards (we consider the case of $B_\phi > 0$ without loss of generality.), generating a vertical current given by equation (2).

When a weak vertical field is applied in addition to the toroidal field the vertical charge separation is relaxed by a return current along the helical field lines. Without

such a return path in the plasma an electric field would evolve and the radial $E \times B$ drift might sweep the plasma away and terminates the discharge. This is just an intuitive picture often employed in elementary literatures on toroidal plasma confinement to emphasize necessity of rotational transform, by asserting that the simple toroidal field provides no equilibrium for the plasma. In many experiments mentioned above, however, the discharges were easily initiated by microwave power and the plasma was maintained as long as the microwave power was fed, suggesting that there is an equilibrium even in these ECR plasmas. Elementary literatures have considered only the transient case in which a cloud of plasma abruptly appears in the toroidal field. They have not considered the case of steady ECR plasmas surrounded by the conducting wall. Primal purpose of the present paper is to find out in what way the ECR plasma is maintained in the presence of the vertical charge separation drifts between electrons and ions.

The conducting vessel provides a return path for the vertical charge separation current as predicted in [17] and confirmed in [18]. In order to complete the current circulation an equal amount of current must flow through the two plasma-wall interfaces at the top and bottom of the chamber. It is conjectured that the VTF-drift electrons reach the bottom, flow into the conducting vessel, go up through the vessel to the top surface, on which they recombine with the ions that flow up from the plasma. Any imbalance of these two currents of electrons and ions causes charge accumulation in the plasma, indicating that a balance is always reached between the two currents carried by different signs of charges in the steady ECR discharges.

This looks, at a first glance, impossible as far as we take only the VTF drifts of electrons and ions into account since the electron temperature is much higher than the ion temperature in ECR plasmas and the electron current and ion current predicted by equation (2) are much different. Net charge would accumulate in the plasma unless electrons emitted freely into the plasma from the ion-side wall. While electrons flow freely into the conducting wall, the reverse is prevented since they must overcome the potential gap (work function) to get through the wall surface out into the plasma. Thus, there arises most important question; what makes the two currents of electrons and ions balanced ?

Previous experiment in the LATE device [19] showed that a cross-field potential hill arises in the ion VTF-drift side (upper side) above the mid-plane on the poloidal cross section. The equipotential contours near the conducting boundary are almost parallel to the boundary. Therefore, the E-fields are like spokes of a wheel from the potential peak to the boundary. Then the $E \times B$ drifts along equipotential contours which also shift to the upper side would convoy the ions from the source belt along the ECR layer to the vicinity of the top wall. Once the ions reach this area their VTF drift would be enhanced on a steep down slope of potential toward the top wall as predicted in [19].

While the experiment [19] was useful to make the rough picture outlined above, it was difficult to advance the picture to a reliable level since two large local limiters were attached at the top and bottom walls in the experiment. Obviously, they violate axi-symmetricity of the plasma. It is too difficult to investigate the situation in non-

axisymmetric configuration. Therefore, we fabricated an axisymmetric configuration with new electrodes and various new diagnostics in the LATE device as described in section 2, and have done new experiments and analyses as presented in section 3. In particular we have found that the electron flow onto the bottom wall (panel) is consistent with the electron VTF drift current predicted by equation (2) and shown that the picture for the same amount of ion current onto the top wall (panel) is the case. Some discussions are given in section 4. The results are summarized in section 5.

2. Experimental apparatus

Figures 1 and 2 show the LATE device with various attachments for present experiments. The vacuum vessel is a cylinder with an inner diameter of 100 cm and an inner height of 100 cm. The center post is also a cylinder with an outside diameter of 11.4 cm, enclosing 60 turns of copper conductors for the generation of a toroidal field. Therefore, major and minor radius of the device is 28 and 22 cm, respectively. Both the vessel and the center post are made of stainless steel and connected without electrical insulation. While there are four sets of poloidal field coils to generate vertical magnetic fields, they are not used in the present experiment.

By taking advantage of the low-aspect-ratio cylindrical space of the rectangular cross section, we have installed top and bottom panels to collect the vertical charge separation current. The panel consists of 12 trapezoidal plates attached to a common frame. Because of the low-aspect-ratio feature, the panels have a large area and almost cover the floor and the ceiling of the vacuum vessel. Therefore, the interaction between the side walls of the vacuum vessel and the plasma is relatively small. A radial array of small electrodes is embedded on each panel as shown in figure 2 to observe the profile of the vertical current flowing into or out from the panel. The panels and the radial electrode array are made of stainless steel.

The energy spectra of ions accelerated onto the top panel is measured using an ion energy analyzer as depicted in figure 1. The analyzer is positioned just behind an arced mesh slit on the top panel.

Degree of perpendicularity of the ceiling and the floor of the vacuum vessel to the center post is excellent. Deviation from $\pi/2$ radian is less than 1/2000 radian. Therefore, the top and bottom panels were adjusted to be parallel to the vessel floor to keep the boundary at the bottom and top axisymmetrically. The results were as follows. The average height of 36 sampling points on the top panel is 297.7 (797.7) mm from the mid plane (the floor) with the mean square root deviation of 0.45 mm and the largest deviation of 1.2 mm. The average height of 24 sampling points on the bottom panel is -300.2 (199.8) mm from the mid plane (the floor) with the mean square root deviation of 0.43 mm and the largest deviation of 1.3 mm.

There are three major conducting walls which surround the plasma, that is, the bottom panel, the top panel and the vacuum vessel wall as seen in figure 2(c). The currents flowing into these walls are much larger than the currents flowing into other

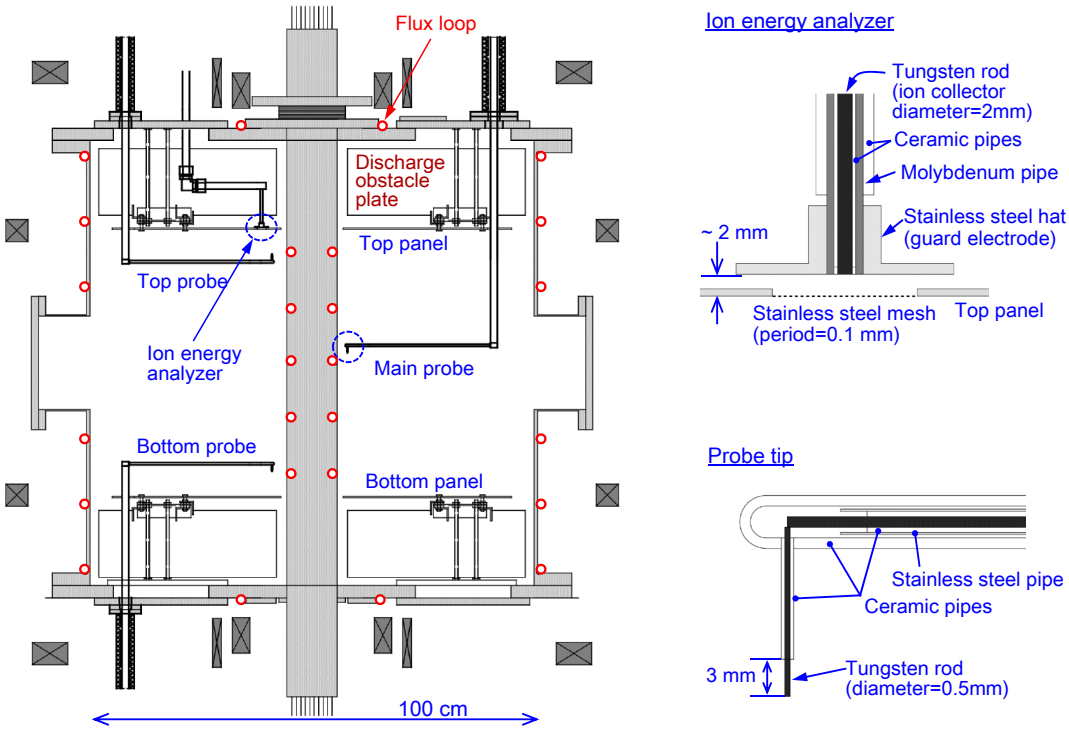

Figure 1. Side view of the LATE discharge chamber for the present experiment with enlargements of the ion energy analyzer and the probe tip. Discharge obstacle plates suppress the ECR discharge behind the top and bottom panels [19].

small electrodes and are detected using resistors with low resistivity (0.1Ω) as shown in figure 3. Since the vacuum vessel is electrically grounded, these three resistor lines are connected at a floating junction. Other small electrodes including the top and bottom electrode arrays, the top and bottom obstacles, three Langmuir probes and the ion analyzer are all connected to the ground point through pickup resistors with higher resistivity as shown in figure 3. Thus all the currents from the plasma into the electrodes and the vessel can be monitored. The observed currents to the panels are less than 4 A. Therefore, potential drops through the current pickup resistors are less than 0.4V, which are negligible compared with the potential difference between the plasma core and the vessel. Each radial electrode array can be switched to a voltage sweeper to obtain voltage-current characteristics.

Three Langmuir probes were used. Each one is rotated by a motor around its vertical axis and is also slid vertically by another motor. Thus the probe tip covers the whole range from R = 90 to 490 mm, and also from Z = 150 to 294 mm by the top probe, from Z = −200 to 200 mm by the main probe and Z = −150 to −296 mm by the bottom probe for the measurement of the profiles of electron density and temperature and the space potential on the poloidal cross section. Furthermore, the line-integrated electron densities along two chords on the mid-plane that have tangential radius of R_t=12 cm and 28 cm, respectively, are measured by 70 GHz interferometers. The data are used to

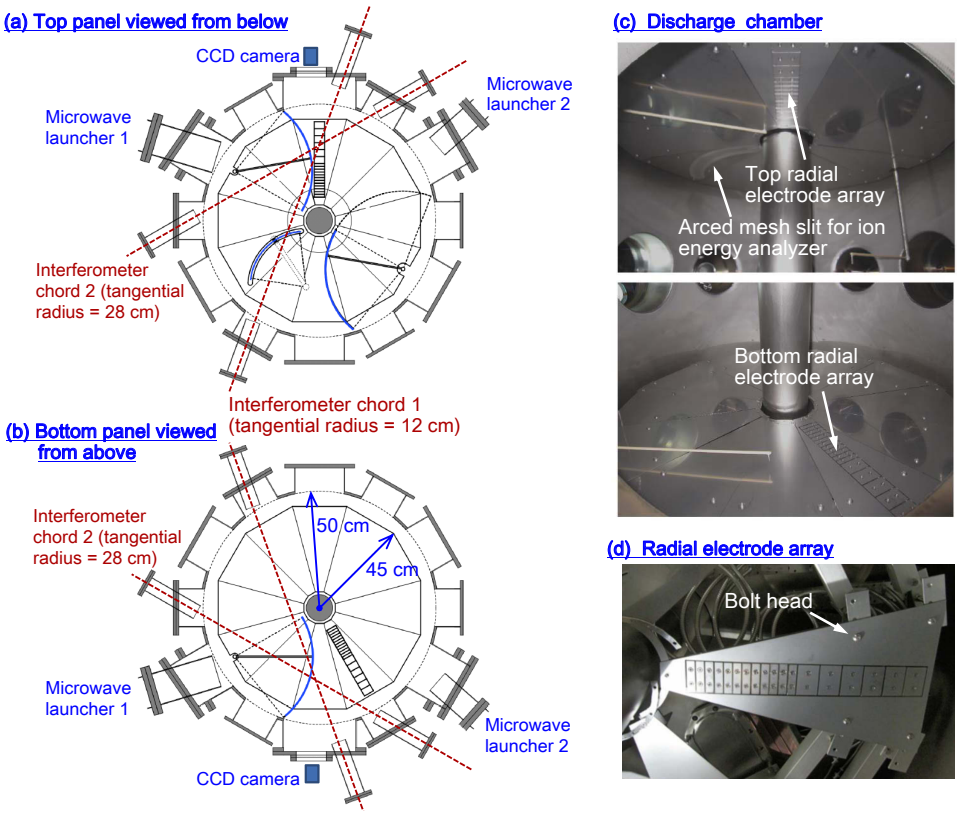

Figure 2. (a) Top panel viewed from below, (b) bottom panel viewed from above (c) photo of discharge chamber between the top and bottom panels and (d) detail of radial array of electrodes on the top and bottom panels.

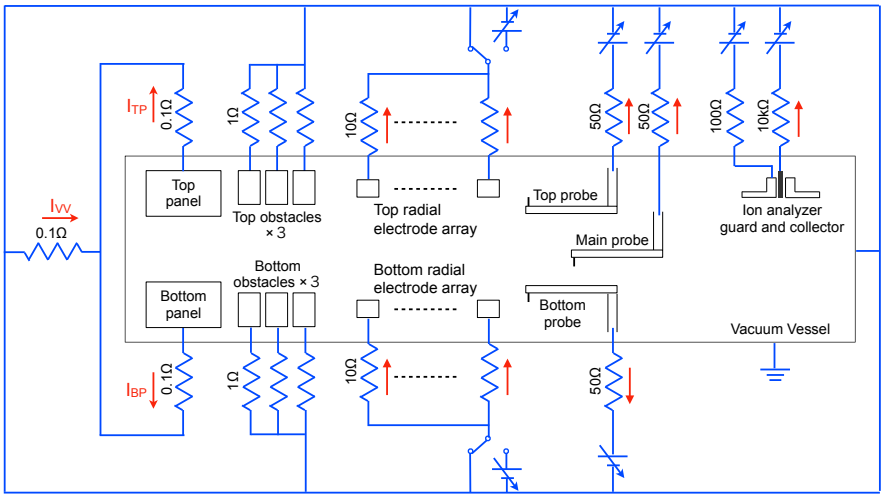

Figure 3. Circuit diagram for various current measurements. The current direction denoted by red arrows is defined to be positive. Note that the definition is reversed between the bottom-panel current I_{BP} and the bottom electrode array currents.

calibrate the electron density profile from the probe measurement.

Microwave power in the range of 0.5-2.0 kW at 2.45 GHz from a magnetron (5 kW, CW) or another magnetron (20 kW, 2 sec) is injected by one of two launchers at different radial ports as shown in figure 2. The launchers are of an open circular waveguide. The angle between the axis of the launchers and the toroidal field is 80 degree at the injection point of R = 50 cm and the wave is linearly polarized with the electric field parallel to the horizontal plane, indicating that the wave is injected almost in the form of O mode. The toroidal field is B_ϕ = 480 G at R = 25 cm and the ECR layer is R_{ECR} = 13.7 cm throughout the paper. The direction of B_ϕ is counterclockwise when it is viewed from top. The working gas for discharges is hydrogen or argon and the detail is described in section 3.1 (see also figure 4).

Finally information on the toroidal plasma current is obtained using the flux signals from the 13 flux loops shown in figure 1.

3. Experimental results and analyses

3.1. Overview of the experiment and observation

Four different ECR discharges, hydrogen discharges by microwave injection power of P_{inj}=0.5, 1.0 or 1.9 kW and an argon discharge by P_{inj}=1.2 kW have been done as shown in figure 4. The argon discharge is for investigation of the effect of finite ion Larmor radius. The discharge duration for the 1.9 kW hydrogen discharge is 2 s and that of the other discharges is 2.5 s. In the former case the microwave from the 20 kW magnetron has been injected through the launcher 1 and in the latter discharges the microwave from the 5 kW magnetron has been injected through the launcher 2 (see figure 2).

In all cases the sequence of operation for discharge is the same. First, the toroidal coil current is ramped up and then kept constant by a transistor power supply to produce the ECR layer for 2.45 GHz at R_{ECR} = 13.7 cm (B_ϕ = 480 G at R = 25 cm). Second, a puff of gas is introduced into the chamber having the base pressure of $\approx 1 \times 10^{-5}$ Pa to fill up the gas around a pressure of $p_{H2} = 3 \times 10^{-2}$ Pa or $p_{Ar} = 1 \times 10^{-2}$ Pa. Third, a microwave pulse is injected. Then the breakdown takes place immediately and a toroidal plasma appears quickly as seen on the signal of the line electron density. The hydrogen gas pressure gradually decreases and reaches the steady pressure of 1.0×10^{-2} Pa after a transition time of ≈0.6 s. Then, the pressure is kept constant by an additional weak gas puffing. In the argon case it takes more time (≈1.2 s) to reach the steady pressure of 5×10^{-3} Pa.

In all discharges, a very small amount of toroidal current is more or less detected throughout the discharge.

The currents flowing into the panels and vacuum vessel during the discharge are shown in the figure 4. I_{TP}, I_{BP} and I_{VV} represent the currents that flow into the top panel, the bottom panel and the vacuum vessel, respectively (see figure 3). All

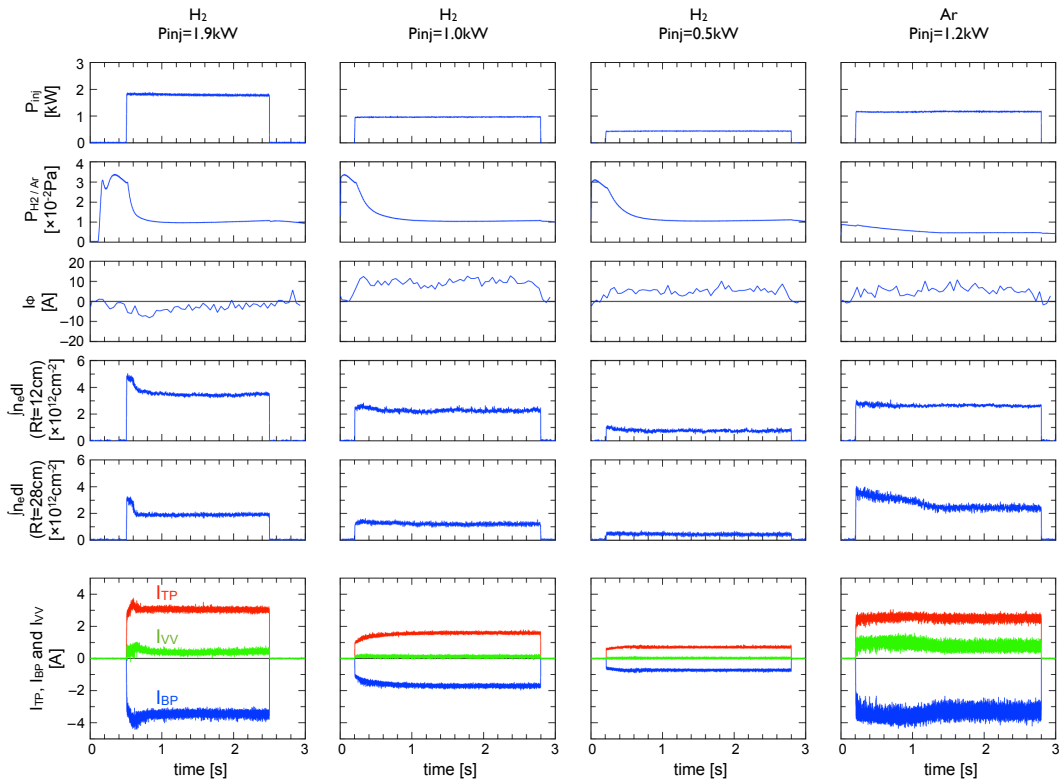

Figure 4. Discharge wave forms. From top to bottom: injected microwave power, gas pressure, toroidal plasma current, line densities on mid-plane chords with tangential radii of R_t=12 cm and 28 cm, the currents flowing into the top panel, vacuum vessel and bottom panel.

the currents become steady after the initial transition time. The sign for these three currents is defined positive for the current direction of flowing into the conductor from the plasma throughout the paper (see figure 3). Here, the toroidal field direction is counter-clockwise when viewed from the top ($B_\phi > 0$) and the electron VTF drift direction is downward.

The bottom panel current I_{BP} is negative, suggesting that this current is mainly due to the electrons that VTF-drift downward. On the other hand, the top panel current I_{TP} is positive, showing that this current is mainly due to ions that drift upwards and reach the top panel. The amount of vessel current I_{VV} is much smaller than I_{BP} and I_{TP} in the hydrogen discharges, while it is significant in the argon discharge. The relationship $I_{BP}+I_{TP}+I_{VV}=0$ is indeed always held within the accuracy of current measurement of $\approx$0.01 A. The above results indicate that in the cases of hydrogen discharges the current flowing into the top electrode is almost returned to the bottom electrode through the external circuit, completing current circulation of the vertical charge separation current. Note that the vacuum vessel current I_{VV} includes the radial electrode array currents and the obstacle currents in addition to the 'true' vessel current (see figure 3). Usually the top and bottom radial electrode array currents cancel out each other and sum of

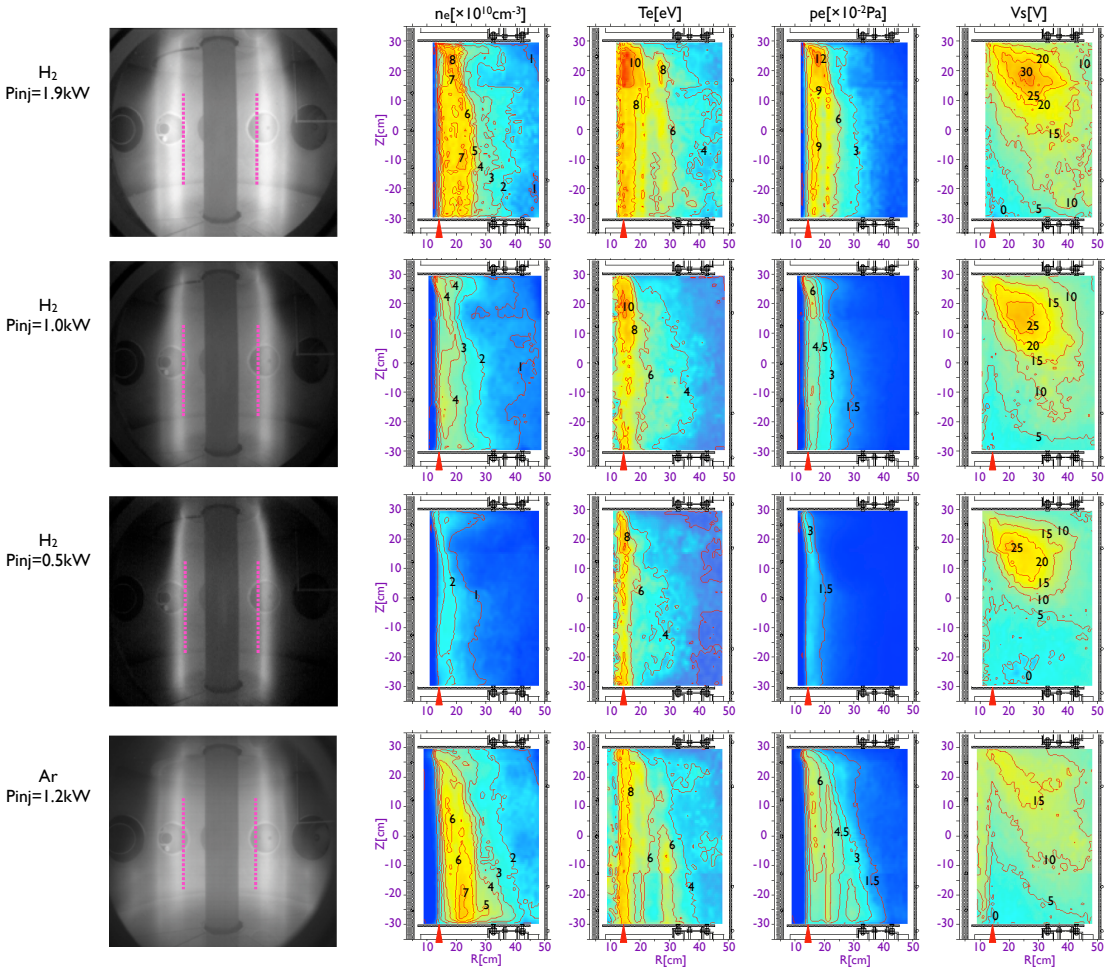

Figure 5. CCD plasma images and plasma profiles (electron density (n_e), temperature (T_e), pressure ($p_e = n_e T_e$) and the space potential (V_S)) during the steady phases of four discharges in figure 4. In each profile the number on the contour line denotes the level in the unit written in the square bracket [ ] on the very top. Pink dotted lines and red triangles show the location of the ECR layer.

these currents is much smaller than I_{VV}. The 'true' vessel currents for the cases of 0.5, 1.0 and 1.9 kW hydrogen discharges and 1.2 kW argon discharge are, 0.04, 0.11, 0.33, and 0.93 A, respectively, while I_{VV}=0.03, 0.09, 0.27, and 0.74 A, respectively.

CCD images of plasma and various plasma profiles on the poloidal cross section during the steady duration in the four discharges in figure 4 are shown in figure 5. The plasma profiles include profiles of the electron density (n_e), temperature (T_e), pressure ($p_e = n_e T_e$) and the space potential (V_S) measured using the Langmuir probes.

Each image shows a vertical emission belt along just lower field side of the ECR layer. The belt resembles the electron pressure profile, which has a vertical ridge that is just coincident with the bright zone of the CCD image. It is remarkable that vertical uniformity of the pressure profile is better than that of density and/or temperature profiles. The density and the temperature compensate each other to make their product

n_eT_e to be more uniform along the vertical pressure ridge.

The potential and pressure profiles are asymmetry along the vertical direction. The same asymmetry was also observed in previous experiment [19], where the profiles were turned upside down like a mirror image on a horizontal flat mirror when the toroidal field was inverted. On the other hand, CCD images in the figure suggest that axi-symmetricity of the plasmas is excellent.

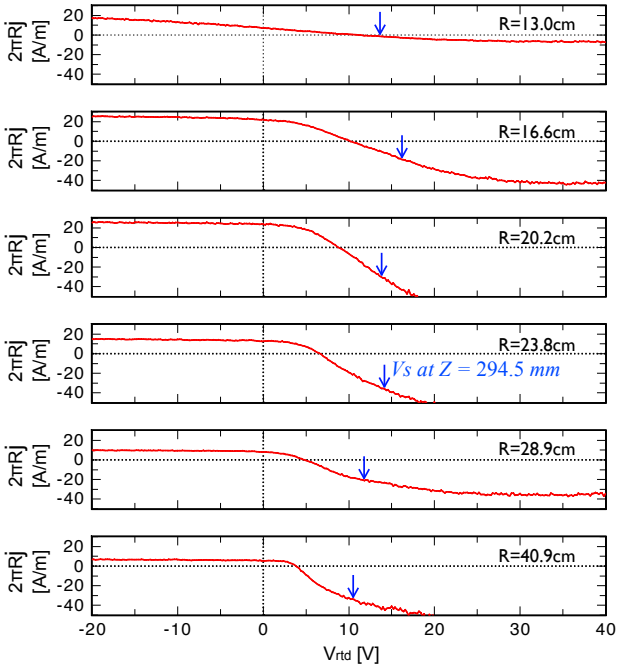

Figure 6. Voltage-current characteristics of the top electrode array in the case of the 1.9 kW hydrogen discharge. Blue arrows indicate the space potential just below the top panel at each R-position.

There arises a positive cross-field potential hill in the upper side on the plasma cross section. In the hydrogen discharges the hill evolves as P_{inj} is increased. Upper left corner of the hill locates at the cross point of the ECR layer and the top panel. From this corner the potential increases along the down and lower field direction toward the peak at $Z \approx$15 cm and $R \approx$25 cm and then decreases along the same direction toward the vessel wall. The peak potential is $V_S = 25 \sim 30$ V and the peak electron temperature is $T_e = 8 \sim 10$ eV in the three hydrogen discharges, while the peak electron density increases from $n_e \cong 2 \times 10^{10} cm^{-3}$ to $8 \times 10^{10} cm^{-3}$ as the microwave injection power increases from P_{inj}=0.5 to 1.9 kW. These results suggest that the peak potential does not depend on the electron density. While the difference in appearance between the profiles of electron pressure and space potential is remarkable, they are closely linked at the corner formed by two lines of the top panel and the ECR layer, suggesting close relationship between them.

The very tip of the tungsten rod is only 2 mm below the top panel in the case

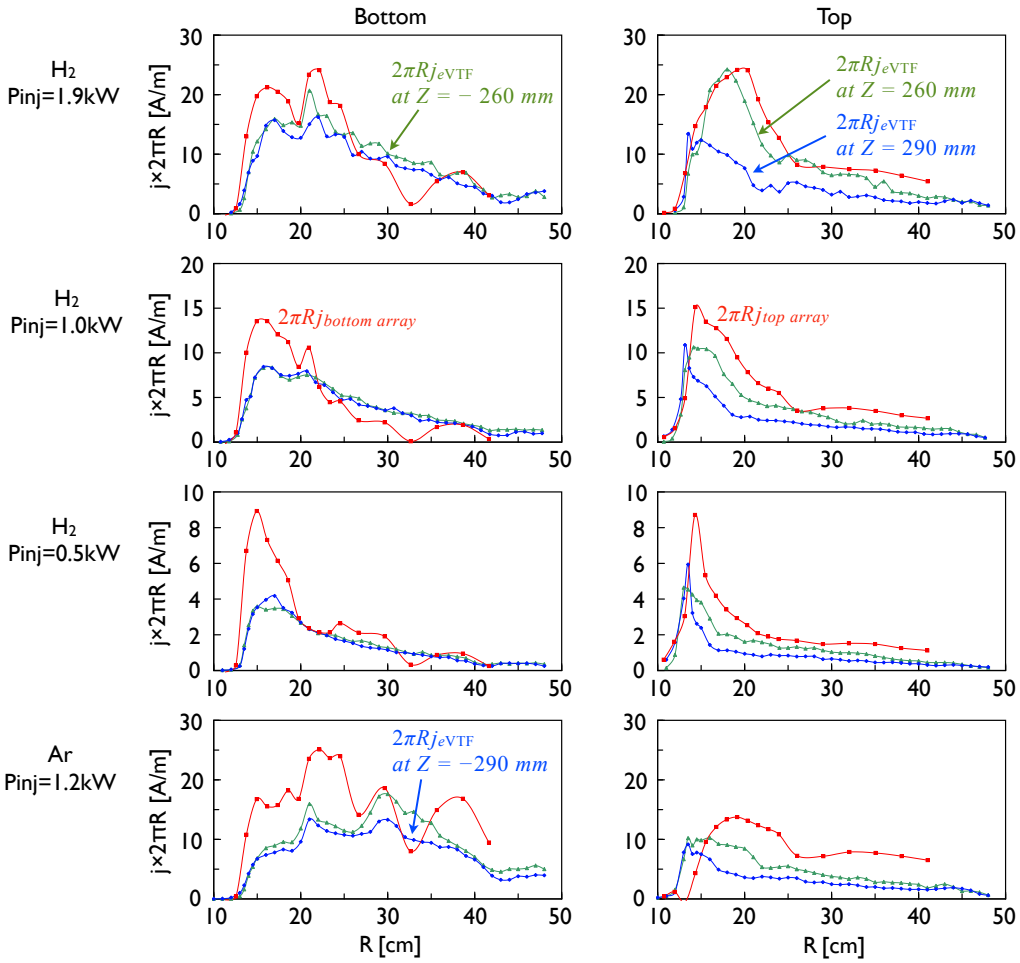

Figure 7. Radial profiles of the vertical current density on bottom and top radial electrode arrays are compared with the radial profiles of electron VTF drift current density estimated from the electron pressure profiles (see equation (2)).

of the uppermost probe measurement. The exposed length of the tungsten rod is 3 mm. Therefore the uppermost location of the center Z coordinate of the probe tip is 3.5 mm below the top panel surface. The potential has been found to be quite high even at this vicinity of the top panel. The value is higher than 10 V except for the case of hydrogen 0.5 kW discharge, suggesting an ion dominant sheath with a very steep potential slope down to the top panel. Hereafter the center Z coordinate is referred to as the Z coordinate of the probes.

The vertical uniformity of the electron pressure in the argon discharge is not quite high as those in the hydrogen discharges, corresponding to the relatively large vessel current I_{VV} shown in figure 4. Even in hydrogen discharges the vertical uniformity deteriorates near the top panel, where the pressure ridge becomes somewhat narrow and slightly kinks towards the higher field side. In particular, the electron pressure decreases strongly toward the top panel at the vicinity of the panel, while there is no

such marked decrease downward to the bottom panel. These points are described in detail in sections 3.5, 3.6 and 3.7.

Figure 6 shows the voltage current characteristics of the top radial electrode array during the 1.9 kW hydrogen discharge. The currents are positive when the retarding voltage is $V_{rtd} = 0$, corresponding to the upward VTF drift of ions. Blue arrows denote the space potential at Z=294.5 mm (3.5 mm below from the panel surface) which is, hereafter, referred to as the ion sheath potential. While the floating voltage of the array electrode most rises to V_f=10 V at rather wide radial location of $R = 14 \sim 17$ cm, the voltage is lower than the ion sheath potential. There is no appreciable current increase when the retarding voltage is decreased from the ground level except for the electrodes located higher field side of the ECR layer, suggesting no secondary electron emission from the array electrodes upon hitting of the ions.

Red plot in figure 7 shows radial profiles of the current density on the bottom and top radial electrode arrays for the cases of four discharges in figures 4 and 5. In each case of discharge the current density in the figure is the value at the retarding voltage equal to the corresponding panel voltage. Note that the voltage of each panel more or less shifts from the ground level due to the voltage across the current pick up resistor. While main current carriers are different between the top and the bottom, both profiles are nearly the same in the hydrogen discharges. This is not the case in the argon discharge, corresponding to the significant vacuum vessel current shown in figure 4. The dip at R=32.5 cm on the bottom array current profiles may be due to the presence of bolts at this radial location (see figure 2), suggesting that the electrons flow fast along the field lines into the bolt head. While there are bolts at the same radial location on the top panel there is no dip on the current profiles onto the top radial electrode array.

The result of current versus retarding voltage of the ion collector of the ion energy analyzer (see figures 1 and 2) just behind the mesh slit during the 1.9 kW hydrogen discharge shows that high energy ions up to 17 eV flow into the top panel around R =16 to 20 cm. The mesh is fine enough to keep the same electrostatic boundary condition as the top panel to the ions that flow onto the panel surface by the steep potential slope of the ion dominant sheath.

3.2. Examination of Langmuir probe measurement

The Langmuir probe measurement has been done on a large number of points on the poloidal cross section, approximately 14 thousand points (200 radial locations $\times$ 69 vertical locations), to cover the whole area to make contour plots as those in figure 5. The radial scan is done in three steps from $R = 49$ to 36 cm, 36 to 22 cm and 22 to 9 cm using one discharge for each step. We sweep the probe voltage sawtooth-likely many times during scan to obtain single probe characteristics within a negligibly small change of R location of probe tip, $\triangle R \approx$0.2 cm.

Z locations of probe scan in terms of Z-coordinate of the center of 3mm-long tungsten rod exposed to the plasma are -296, -295, -290, -280, $\cdots$, 240, 250, 255, $\cdots$,

285, 290, 292, 293.5, 294.5 mm. The range from −290 to 250 mm is scanned by 10 mm step and the range from 250 to 290 is scanned by 5mm step. The range from −296 to −140 mm is measured using the bottom probe, the range from −130 to 150 mm using the main probe and the range from 160 to 294.5 mm using the top probe. Note that the bottom panel location is −300mm and the top panel location is 298 mm.

Usually, two of the three probes positioned at two different Z coordinates have simultaneously done radial scans during one discharge. Simultaneous scans from R=22 to 9 cm have been avoided since the disturbance to the plasma becomes significant.

While T_e and V_S are measured with relatively high accuracy from the probe V-I characteristics, there is a concern about the accuracy of the density measurement since it depends on the validity of the effective cross section of the probe surface employed for the analysis. Another concern is a possible disturbance from the probe insertion deep into the plasma. We have examined these points by comparing the probe result with the interferometer result as shown in figure 8.

In every case there is a discrepancy between two kinds of line integrated density, one from the interferometers and another from the probe results denoted by grey lines. Here twice the cross section of the exposed tungsten rod of the probe intersected by the field lines, $S = 2d\ell$ (d and ℓ being the diameter and the length of the rod, respectively) is initially used for the density analysis. Then we have adjusted the probe results so that they become equal to the interferometer results by modifying the probe cross section by introducing a correction factor α as follows

$$S \rightarrow S_{eff} = 2\ell d(1 + \alpha\rho_e)$$

Here ρ_e is the local electron Larmor radius. The results are denoted by purple lines in figure 8. The density and pressure profiles in figure 5 are plotted after these adjustments.

First we considered that the electrons would flow into the probe surface along the field lines with making Larmor motions and then the effective cross section should be somewhat larger than the probe cross section, since ρ_e=0.13 mm for T_e=8 eV and B_ϕ=800 Gauss, typical value in the experiment, is significant compared with the probe tip diameter of 0.5 mm. However, the correction factors are much different between the four discharge cases in figure 8. Furthermore, we have made a similar comparison between the interferometer and probe results for the case of a 2 mm diameter tungsten rod. In this case the probe line integrated density is lower than the interferometer value by $\cong$ 30% for the 1 kW hydrogen discharge when we use $S = 2d\ell$ for the cross section. These results suggest that our first simple model do not quite work in the probe current correction. In particular in the 0.5 kW hydrogen discharge case the correction is significant, suggesting that other unknown factors may affect the current collecting.

The comparison between the profiles of the bottom radial electrode array current and the electron VTF drift current estimated using equation (2) is shown in figure 7, which may provide another information on reliability on the probe measurement. There is a significant discrepancy between the peak current densities at $R \sim$15 cm in the cases of the 0.5 kW hydrogen discharge plasma. The excess portion of the array current over

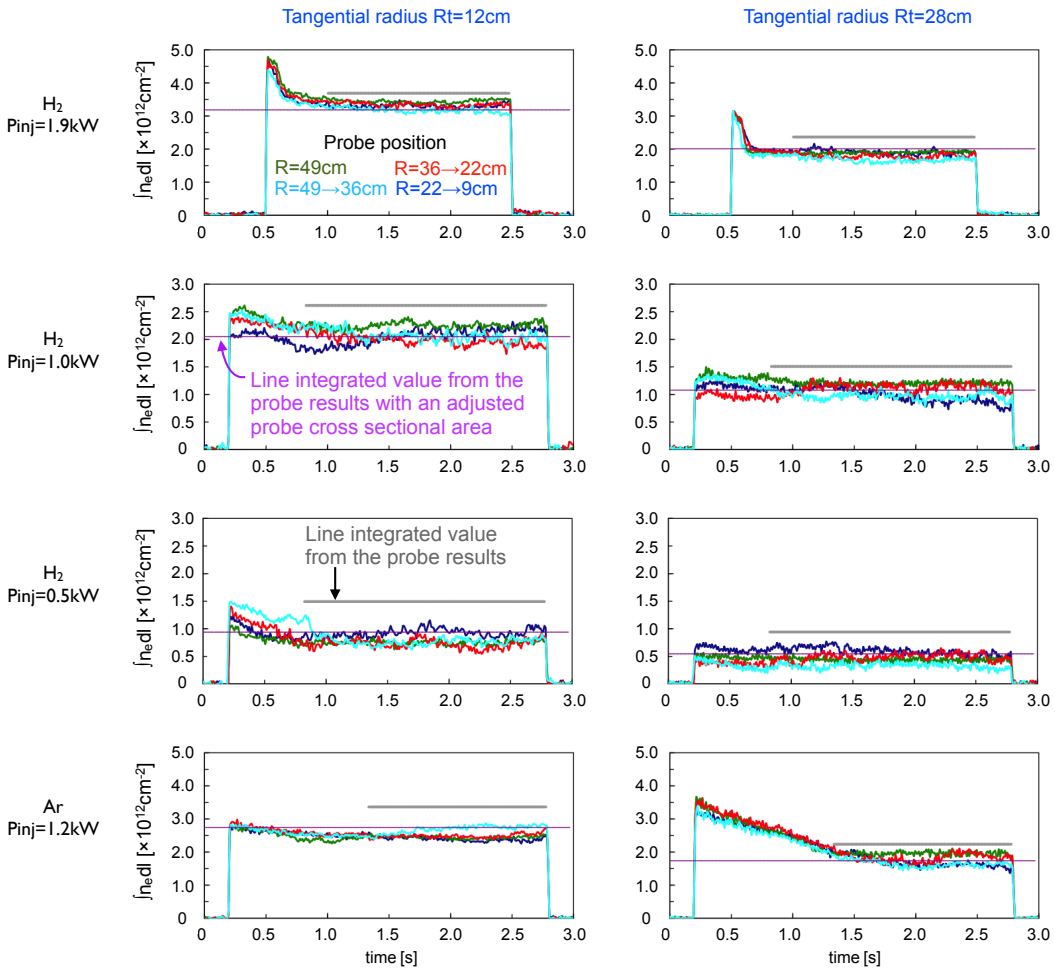

Figure 8. The line integrated values along two chords of $R_t = 12$ cm and 28 cm from 70 GHz interferometers and probe results are compared during the time spans of the grey lines during which the scanning probe measurements are done. The effective probe cross section for the density estimation is adjusted to the values from the interferometers as described in the main text.

the VTF drift current of the bulk electrons may be due to the energetic electrons which are EC-heated perpendicularly to the field line. In this plasma the electron density is low and the collision time is long ($\tau_{ei} = 40\mu$s when $n_e = 2 \times 10^{10} cm^{-3}$ and T_e=10 eV) and then an anisotropic velocity distribution may evolve as described in section 3.4. While there is no indication on the probe V-I characteristics for such an electron tail, perpendicular tail electrons are undetectable since the probe can collect electrons only along the free streaming direction of the field lines. On the other hand, both profiles in the 1.9 kW hydrogen discharge plasma relatively well coincident each other.

Small toroidal current I_ϕ in figure 4 suggests presence of such an energetic electron tail. The LATE device has an error vertical field of $B_Z \cong -0.2$ Gauss in present experimental condition. These collisionless energetic electrons would return along the helical field lines as described in section 1 and generate a toroidal current. The ratio

I_ϕ/I_{BP} is most large in the 0.5 kW hydrogen discharge and most small in the 1.9 kW hydrogen discharge.

The results described in above three paragraphs indicate that the probe results in the 1.9 kW hydrogen discharge plasma are most reliable. Furthermore, the disturbance from the probe insertion is most small on the interferometer signal in the 1.9 kW hydrogen discharge as shown in figure 8. Therefore we mainly use the 1.9 kW hydrogen results for further analyses in the following sections.

3.3. Electron flow from source to boundary

Typical parameters of the 1.9 kW hydrogen discharge plasma in figure 5 are the followings: $n_e \approx 7\times10^{16}$ m^{-3}, $T_e \approx 8$ eV, $V_S \approx 30$ V, $E \approx V_S/plasma\ radius \approx 30$ V/0.25 m= 120 Vm^{-1}, p_{H2}(hydrogen pressure)$\approx 1\times10^{-2}$ Pa, n_{H2}(molecule density) $\approx 2.8\times10^{18}$ m^{-3}, and $B_\phi = 0.0875$ T at the ECR layer $R_{ECR} = 0.137$ m. Using these values various parameters and characteristics are estimated as follows.

The electron pressure is $p_e \equiv n_eT_e \approx 0.1$ Pa and the magnetic pressure is $p_{mag} \equiv B_\phi^2/2\mu_0 \sim 10^3$ Pa. The VTF drift velocity of thermal electrons is typically,

$$V_{VTF} \approx \frac{2T_e}{eRB_\phi} \approx 1400\ \mathrm{ms}^{-1}.$$

When we used the strength of toroidal field at $R = 0.16$ m, the $E\times B$ drift velocity is typically,

$$V_{E\times B} = E/B \approx 120/0.075 \approx 1600\ \mathrm{ms}^{-1},$$

being nearly the same velocity as the electron VTF drift velocity. Then, the time needed for thermal electrons to traverse the plasma cross section is typically,

$$\tau_{trv} = \frac{plasma\ radius}{V_{drift}} \approx \frac{0.25}{1400} \approx 0.18\ \mathrm{ms},$$

where $V_{drift} = V_{VTF}$ *or* $V_{E\times B}$. The electron-ion collision time for thermal electrons is $\tau_{ei} \approx 0.007$ ms, which is much shorter than the traverse time.

The local particle flux density of electrons (ions) are sum of the fluxes due to the $E\times B$ and VTF drifts.

$$\mathbf{\Gamma}_{e(i)} = \mathbf{\Gamma}_{E\times B} + \mathbf{\Gamma}_{e(i)VTF} \tag{3}$$

Here charge neutrality holds at the level of $(n_i - n_e)/n_e \sim 10^{-5}$ as estimated from the V_S and n_e profiles in figure 5 (see also figure 9(l)), and

$$\mathbf{\Gamma}_{E\times B} = n_e\mathbf{u}_{E\times B} = n_i\mathbf{u}_{E\times B},$$

$$\mathbf{u}_{E\times B} = \frac{E_R}{B_\phi}\widehat{Z} - \frac{E_Z}{B_\phi}\widehat{R},$$

$$\mathbf{\Gamma}_{eVTF} = \frac{j_{eVTF}}{-e}\widehat{Z} = -\frac{2n_eT_e}{eRB_\phi}\widehat{Z},$$

$$\mathbf{\Gamma}_{iVTF} = \frac{j_{iVTF}}{e}\widehat{Z} = \frac{2n_iT_i}{eRB_\phi}\widehat{Z},$$

$$E_R = -\frac{\partial V_S}{\partial R} \;\; and \;\; E_Z = -\frac{\partial V_S}{\partial Z}.$$

Here we assume singly ionized ions. The electric current density is given by

$$\mathbf{j} = -e\mathbf{\Gamma}_{eVTF} + e\mathbf{\Gamma}_{iVTF} = \frac{2(n_eT_e + n_iT_i)}{RB_\phi}\widehat{Z} \tag{4}$$

The condition $0 = div\mathbf{j}$ should be fulfilled in steady state, which implies the following relationship,

$$p_e + p_i = const. \tag{5}$$

along the vertical chord.

In order to analyze the electron flows due to the VTF and $E \times B$ drifts on the poloidal cross section we first have done profile-smoothing for the n_e, T_e , p_e and V_S profiles in the case of 1.9 kW hydrogen discharge plasma in figure 5 using appropriate polynomial expressions for coordinates R and Z to fit the smoothed profiles to the measurement results. Figures 9 (a)-(d) are the results, respectively. Figures 9 (f), (g) and (h) show the flows using blue arrows for the local flux density vectors, $\mathbf{\Gamma}_{E\times B}$, $\mathbf{\Gamma}_{eVTF}$ and $\mathbf{\Gamma}_e = \mathbf{\Gamma}_{E\times B} + \mathbf{\Gamma}_{eVTF}$, respectively, where the vectors are weighted by $2\pi R$.

While $\mathbf{\Gamma}_{eVTF}$ has only Z component, $\mathbf{\Gamma}_{E\times B}$ has R and Z components. There is no plasma at $R \leq 12$ cm and, therefore, no electron and ion fluxes across the cylindrical surface that has the radius of R=12 cm. The potential is as high as over 10 Volt just in front of the top panel. Therefore, there would be no electron flux toward the panel. On the other hand there is a large flux toward the bottom panel. Figure 9(h) shows a local $E \times B$ flow toward the side wall of the vessel near the location of $R \approx 48$ cm and $Z \approx -28$ cm. The local source rate of electron is given by $div\mathbf{\Gamma}_e$ and plotted in figure 9(k), which shows that the electrons are produced mainly in the area between the ECR and UHR layers, which is coincident with the pressure ridge shown in figure 9(c).

Based on the particle flow shown in figures 9 (f), (g) and (h), we have calculated the particle flux across the side of the vertical cylinder at R=48 cm and also the particle flux across the horizontal hollow circular disc shown by green and pink lines, respectively, in figure 10(a). The directions of the fluxes indicated by the arrows on the lines are defined positive, respectively. The former flux is horizontal and a function of the Z-coordinate of the cylinder bottom and is defined as

$$\mathcal{H}(Z) = -e\int_Z^{Z'=29cm} \Gamma_{E\times B\_R} 2\pi R dZ' \;\; with \; R = 48 \; cm.$$

Here the flux is multiplied by $e = 1.6 \times 10^{-19}$ C and referred to as 'particle current' for later comparisons with the electric currents onto the top and bottom panels. Note that 'particle current' is the same as the electric current when the carrier is singly ionized

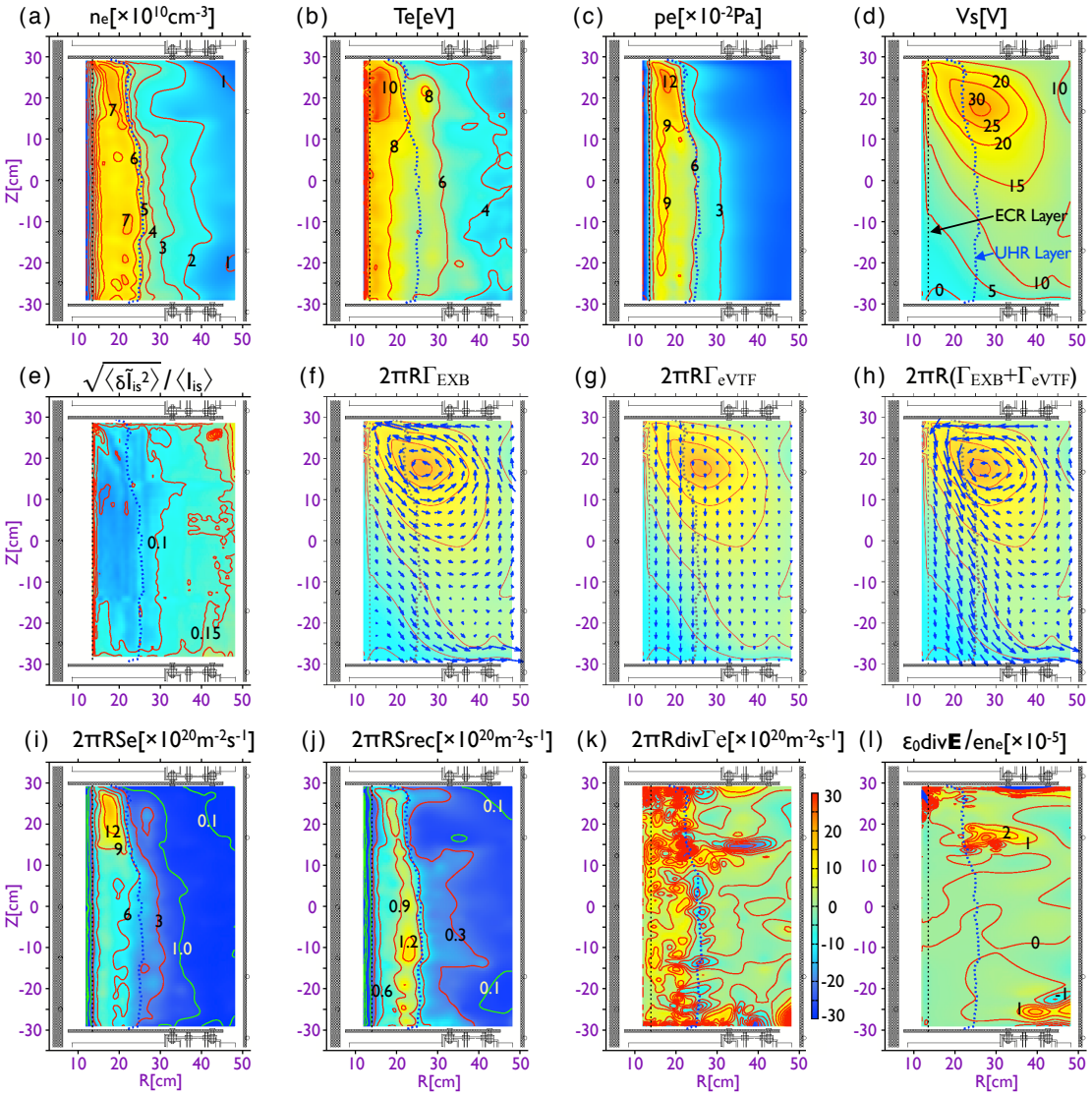

Figure 9. Various profiles in the 1.9 kW hydrogen discharge plasma shown in figures 4 and 5. (a)-(d); Smoothed profiles for the electron density, temperature and pressure, and space potential, respectively. The rest are (e) fluctuation on the ion saturation current, (f) $E \times B$ drift flux density, (g) electron VTF drift flux density, (h) combined drift flux density, (i) source rate of hydrogen molecule ion by electron impact ionization , (j) dissociation rate of hydrogen molecule ion to two hydrogen atoms where all ions are assumed to be hydrogen molecule ion, (k) divergence of combined drift flux density and (l) net charge density normalized to electron charge density. The profiles in (f)-(k) are weighted by $2\pi R$.

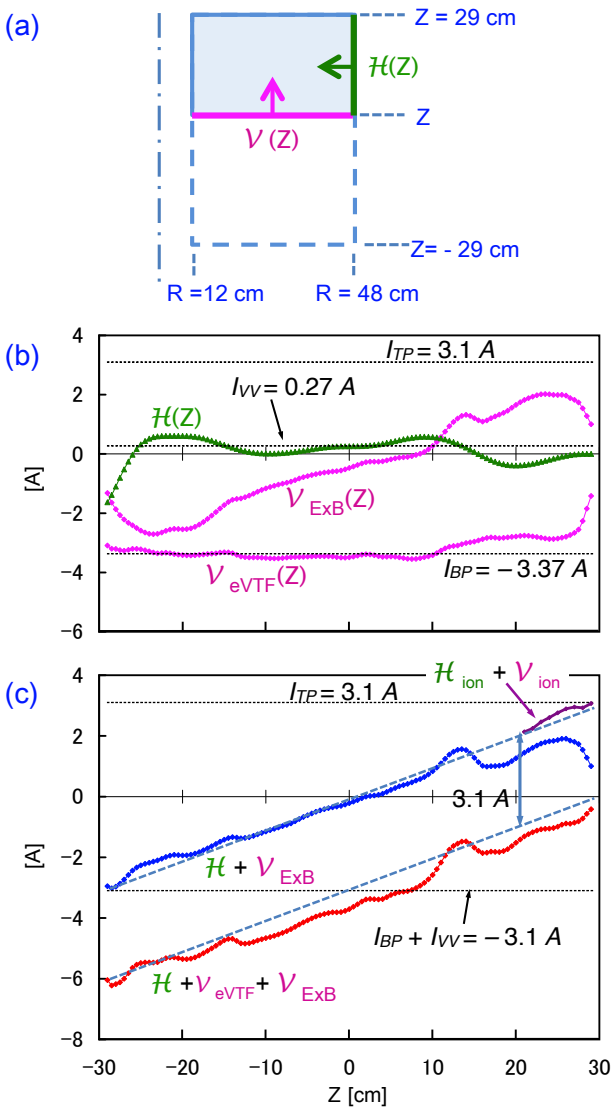

Figure 10. (a) Schematic presentation of vertical and horizontal fluxes $\mathcal{V}(Z)$ and $\mathcal{H}(Z)$ across pink and green boundaries, respectively. (b) $\mathcal{V}(Z)$ and $\mathcal{H}(Z)$ and (c) combined fluxes as functions of Z in the 1.9 kW hydrogen discharge plasma. Ion flux $\mathcal{H}_{ion} + \mathcal{V}_{ion}$ due to $\Gamma_{wi} + \Gamma_{ci}$ in figure 15 is also plotted as a function of Z.

ions while the direction is opposite when the carrier is electrons. The latter vertical flux is also a function of the Z-coordinate of the disc and is defined as

$$\mathcal{V}_{E\times B}(Z) = e\int_{R=12cm}^{R=48cm} \Gamma_{E\times B\_Z} 2\pi R dR$$

and

$$\mathcal{V}_{e(i)VTF}(Z) = e\int_{R=12cm}^{R=48cm} \Gamma_{e(i)VTF} 2\pi R dR.$$

Here subscripts R and Z denote R and Z components of the vector $\Gamma_{E\times B}$, respectively.

They are plotted as functions of Z in figure 10(b). The sums, $\mathcal{H} + \mathcal{V}_{E\times B}$ and $\mathcal{H} + \mathcal{V}_{E\times B} + \mathcal{V}_{eVTF}$ are plotted using the blue and red lines, respectively, in figure 10(c). The latter value at $Z = -29$ cm is $\cong -6$ A. Thus 'particle current' of electrons from the plasma toward the surrounding wall is $\cong 6$ A, which is equal to the total source rate in the plasma. The $\mathcal{H} + \mathcal{V}_{E\times B} + \mathcal{V}_{eVTF}$ line almost linearly increases with Z towards zero at Z=30 cm, the top panel location, indicating that the local source rate is vertically uniform and no electron flux onto the top panel. Note that $\mathcal{V}_{E\times B}$ quickly decreases with Z in front of the top panel. This result suggests that the ion VTF flux $\mathcal{V}_{iVTF}$ must quickly increase to compensate the ion $E \times B$ flux to generate the ion current onto the top panel, $I_{TP} = 3.1$ A. This is described in section 3.5.

The total generation rate of ions should be the same as that of electrons and the top panel current ($I_{TP} = 3.1$ A) is solely due to the ions. The 'particle current' towards the vessel wall is estimated to be ≈ 2 A from $\mathcal{H}$ around $Z = -29$ cm in figure 10(b). Since the electric currents onto the top panel, the bottom panel and the vessel are 3.1, -3.37 and 0.27 A, respectively, the electron (ion) 'particle currents' to the top panel, bottom panel, and the vacuum vessel are estimated to be 0 (3.1) A, 4.27 (0.9) A, and 1.73 (2.0) A, respectively.

The difference between the electron and ion particle fluxes towards the vessel as appeared as the vessel current I_{VV} increases with the microwave power in the hydrogen discharges and it is large in the argon discharge as seen in figure 4. It may have something to do with the large difference between the electron and ion Larmor radii.

3.4. Ion flow from source to boundary

The electron impact ionization cross sections for hydrogen atoms and hydrogen molecules are almost the same [20, 21] and therefore initially hydrogen molecule ions are generated at the high T_e area along the ECR layer. Electron impact ionization rate for molecular hydrogen and electron impact dissociation rates for hydrogen molecular ions are shown as functions of T_e in [20]. These characteristics suggest the following process for generation and disappearance of the ions.

First step: hydrogen molecular ions are generated via electron impact ionization.

Second step: A pair of proton and hydrogen atom or a pair of hydrogen atom at ground state and hydrogen atom at excited state is generated by succeeding electron impact dissociation of hydrogen molecular ion. Note that upon these electron impact dissociations both of the pair particles (proton and hydrogen atom) are separated each other with a kinetic energy of $2 \sim 4$ eV for each [22], while hydrogen molecule ions do not gain kinetic energy upon electron impact ionization.

Remark: Recombination rate of protons with electrons is quite low and the protons survive until they reach the conducting wall on which they are recombined with the electrons.

Figures 9 (i) and (j) show the profiles of electron impact ionization rate for molecular hydrogen and electron impact dissociation recombination rate from molecular hydrogen

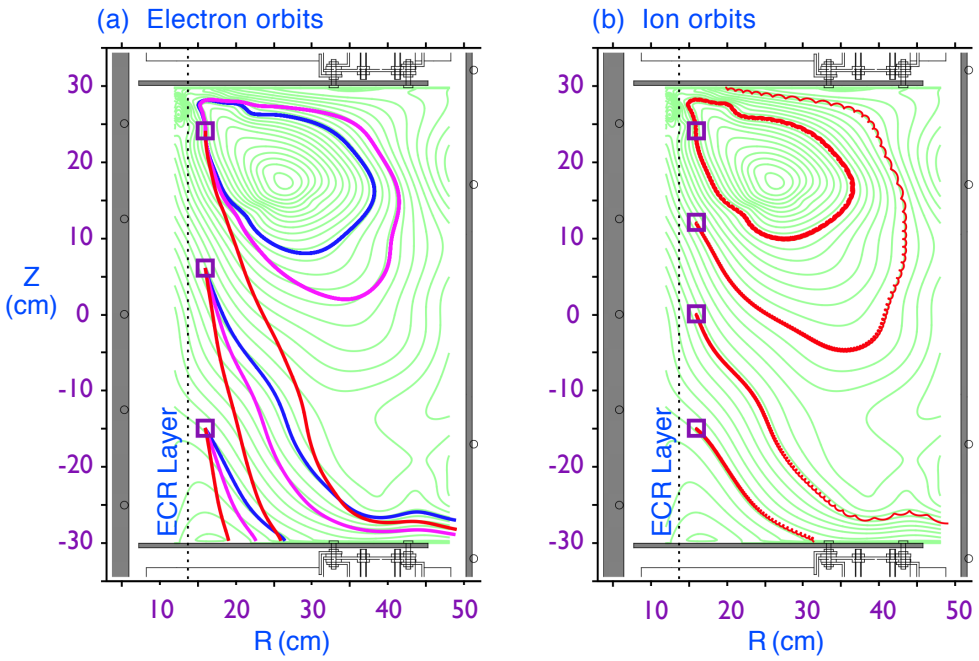

Figure 11. Electron and ion orbits on the V_S contours with 1 V step from the source belt of electron impact ionization to the boundary. No collision included. Initial kinetic energy is 3, 8 and 20 eV for blue, pink and red orbits of electrons and 0.25 eV for hydrogen molecule ions, respectively. Initial pitch angle is 54 degree in every case. Analyses for the 1.9 kW hydrogen plasma.

ions back to the neutral particle, respectively.

Figure 11 shows single particle orbits for the electrons and ions from the source layer to the boundary. No collision is included. Figures 12 (a) and (b) show the electron travel times from the source layer to the boundary walls. The more the electron is energetic its orbit becomes more vertical and it stays more long in the heating zone. In the case of 0.5 kW hydrogen discharge, the e-i collision time is estimated to be ≈ 0.12 ms for a 20 eV electron in the density of $2 \times 10^{10} cm^{-3}$, which is significantly longer than the travel times for the electrons at the source layer near the bottom panel. Therefore, an anisotropic energetic tail to the perpendicular direction in velocity space may develops as appeared as a large enhancement of the bottom electrode array current over the bulk electron VTF drift current in figure 7.

Figure 12(c) shows the travel times of hydrogen molecular ions as a function of Z-coordinate of the source point. On each orbit the molecular ion may dissociate into a proton-atom pair or an atom-atom pair or reach the boundary without dissociation. While the percentages of these events varies depending on the source location, in the end of travel over 50% of molecular ions have been converted into protons as shown in figure 12(e).

Some electrons and ions take closed orbits around the potential hill and do not reach the boundary. Actually they collide with other particles and would eventually get

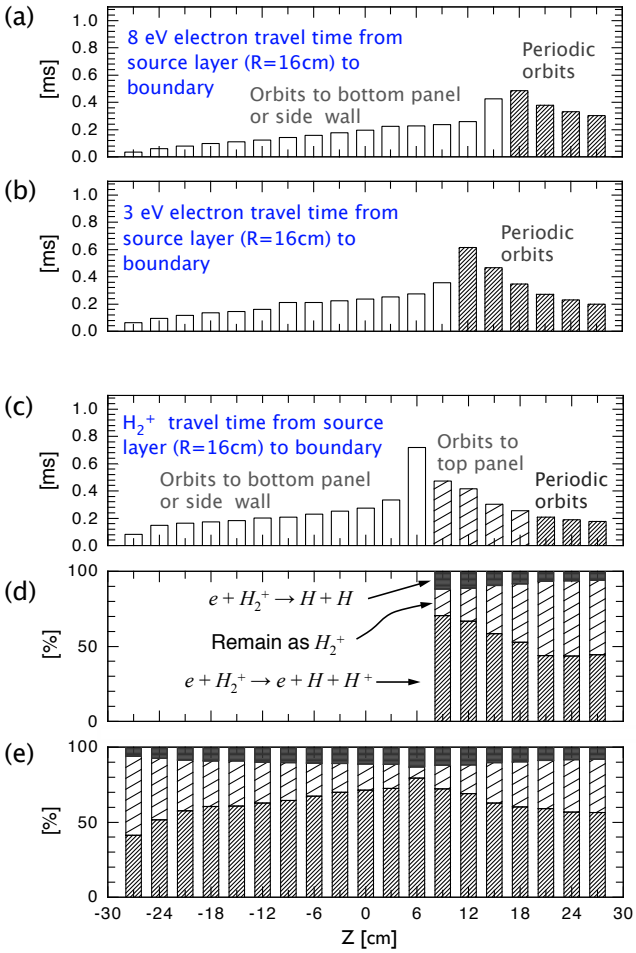

Figure 12. (a)-(c) Travel times of electrons and H_2^+ ions from the source layer of electron impact ionization to the boundary as functions of Z coordinate of the starting point along the source layer at R=16 cm. Travel times for periodic orbits are defined as their periods. (d) Conversion percentages to neutral particles or proton from H_2^+ by electron impact on the way from the source layer to the starting line of R=28-48 cm on Z=20 cm used in the modeling of ion enhanced VTF drift in section 3.5. (e) Conversion percentages to neutral particles or proton from H_2^+ by electron impact on the way from the source layer to the boundary. In the numerical calculation the boundary is set at Z=-296 mm for the bottom panel, Z=294.5 mm for the top panel and R=490 mm for the side wall. Analyses for the 1.9 kW hydrogen plasma.

out from the closed orbit and reach the boundary. The average particle transport time defined as the total 'particle current' across the plasma boundary (≈6 A) divided by the product of total particle number and e is ≈0.3 msec, which is similar to the travel times estimated from the single particle motion in the potential shown in figure 9(d), which is the profile averaged spatially as well as temporally. This result may suggest that there is no significant particle transport due to turbulence. The fluctuation level on the ion saturation current is $10 \sim 15\%$ as shown in figure 9(e).

3.5. Replacement from electron-VTF to ion-VTF current in front of top panel

The area between the potential hill and the top panel is narrow and has a steep potential down slope towards the top panel, where the $E \times B$ drift carries the plasma towards the ECR layer. Here, the electron orbit depends strongly on the kinetic energy as shown in figure 13. Energetic electrons climb up the potential slope as they $E \times B$ drift toward high field side, while low energy electrons $E \times B$ drift almost along the equi-potential contour.

These are single particle orbits without collisions. This behavior is understood based on simultaneous conservation of total energy, the magnetic moment $\mu = m_e v_\perp^2/2B_\phi = m_e R v_\perp^2/2R_0 B_0$ and the angular momentum around the Z axis $L = mRv_\phi$. When R coordinate becomes half, both $v_\perp^2$ and v_ϕ becomes twice, which means the electron climb up the potential slope to increase the kinetic energy by the amount corresponding to the increment that accompanies with the increases of $v_\perp^2$ and v_ϕ for the conservation of the magnetic moment and the angular momentum. Indeed the electrons experience frequent collision and the prediction based on the collisionless orbits is not accurate. Nevertheless, this behavior would remove the thermal energy from the electrons near the top panel. The cold electrons remain and flow toward the ECR layer along the equi-potential contours, which decreases the electron pressure just in front of the top panel near the ECR layer as shown in figure 13(c).

The response of ions to the steep potential slope is opposite to the electron case as shown in figure 14. The ions climb down the potential slope as they $E \times B$ drift toward high field side. When the ions initially have a sufficiently high kinetic energy, they significantly deviate upside from the equi-potential contour and gain the kinetic energy and reach the top panel. Thus the ion pressure would increase as the ions $E \times B$ drift toward the ECR layer and might compensate the decrement of electron pressure in front of the top panel to make total pressure or total VTF drift current unchanged toward the top panel as predicted by equation (5).

Since it is difficult to measure directly the ion temperature profile near the top panel, a numerical simulation based on the single particle motion of ions has been done to see whether or not this effect can compensate the decrement of electron VTF drift current in front of the top panel. We set up a 0.5 cm square grid on the simulation area of a rectangular from Z=20.25 cm to 29.75 cm and R=12.75 cm to 48.25 cm in front of the top panel on the poloidal cross section and calculate the ion density and the current on each square cell contributed from a large number of ions that start from the starting cell array aligned along the starting line from R=27.9 cm to 48.1 cm on Z=20 cm. They are assumed to have a Maxwellian velocity distribution with a same temperature on the starting cell array with the starting density set to be the smoothed density given in figure 9(a).

Figure 15(g) shows the flow profile of the ions with an initial temperature of T_{i_init}=2 eV on the starting cells. Figure 15(b) shows their density profile. The difference from the profile-smoothed electron density shown in figure 15(a) is plotted in figure 15(c),

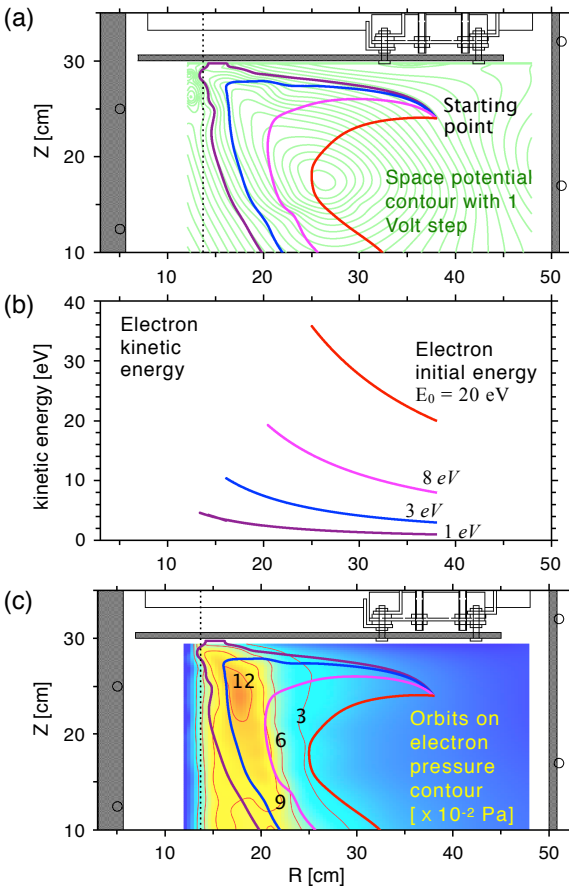

Figure 13. Electron orbits on the steep potential slope between the potential peak and the top panel. Initial pitch angle is 54 degree in every case. Analyses for the 1.9 kW hydrogen plasma.

which may correspond to the density of low temperature hydrogen molecule ions just produced via electron impact ionization. Hereafter we refer to the orbit modeling ions as warm ions (wi) and the rest low temperature hydrogen molecule ions as cold ions (ci). The flow profile of these cold ions is shown in figure 15(h) and the total ion flow profile is shown in figure 15(f). For comparison the electron flow profile is shown in figure 15(e), which is an expansion of figure 9(h).

The result in figure 15(c) is roughly consistent with the source profile shown in figure 9(i) although there appears slightly negative density area for the modeled hydrogen molecule ions. Most negative value is $-0.3 \times 10^{10} cm^{-3}$. When we employ T_{i_init}= 1.0 eV , not only negative area expands but also negative level increases to $-0.6 \times 10^{10} cm^{-3}$. When T_{i_init}=0.1 eV, it increases further to $-3.0 \times 10^{10} cm^{-3}$.

While we do not measure ion temperature in present experiment, we did using an ion sensitive probe in a previous experiment , where a similar ECR plasma having a similar cross-field potential hill was generated [23]. The result showed $T_i \cong$1.9 eV. The energy transfer time from electrons to ions via collisions is too long (≈1.4 sec) to heat

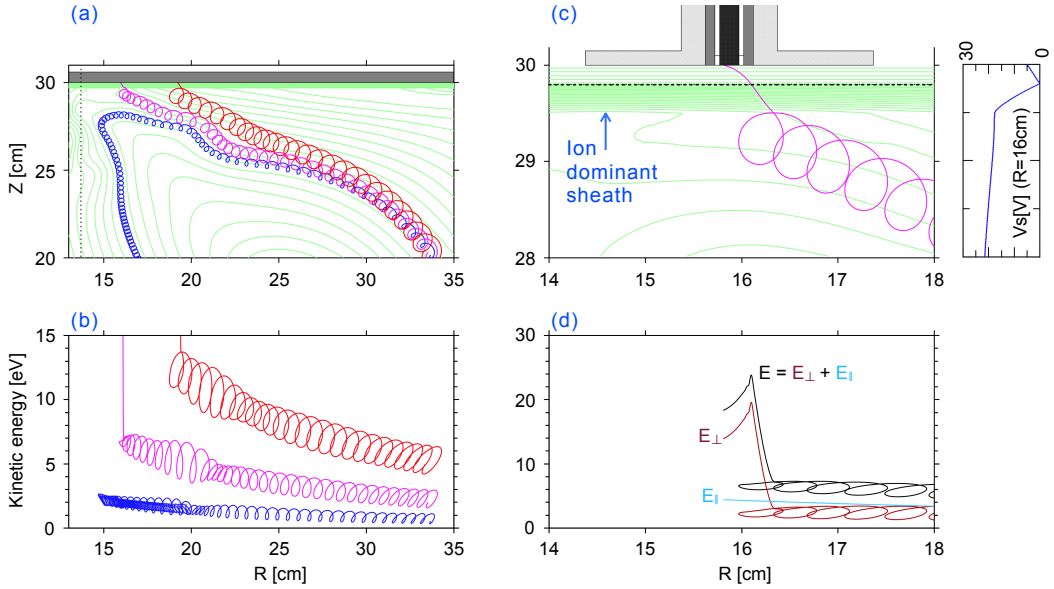

Figure 14. Enhanced ion drifts toward the top panel driven by the steep down slope of potential. Initial pitch angle is 54 degree in every case. Analyses for the 1.9 kW hydrogen plasma.

ions up to this temperature. Most probable origin of ion energy of 2 eV is the electron impact dissociations, in which both proton and hydrogen atom are separated each other with a kinetic energy of $2 \sim 4$ eV for each as mentioned in section 3.4.

Figure 15(d) shows the flow difference between the electron and ion flows shown in figures 15 (e) and (f), respectively. The arrow direction more or less deviates from the vertical direction even in the area apart from the ion dominant sheath. This result indicate that the guiding center approximation is not quite accurate for the warm ions in this area of the steep potential slope. If the approximation is rigorous the $E \times B$ drifts of electrons and ions cancel out each other and only the vertical VTF drifts remain.

The ion 'particle current' fluxes, $\mathcal{H}_i(Z) + \mathcal{V}_i(Z)$ are obtained from figure 15(f) and plotted in figure 10. Present simulation based on the collisionless single particle orbit of ions shows that the current that flows onto the top panel at Z=298 mm is the same as the current at Z=290 mm for various sheath widths from 0.5 mm to 3mm. The result gives the vertical current of 3.0 A to the top panel, being consistent with the observed top panel current of I_{TP} =3.1 A. This is the result with T_{i_init}=2 eV at the starting cell array. When we employ T_{i_init}=1.0 eV and 0.1 eV for the initial temperature, the vertical current to the top panel are found to be 2.6 A and 1.9 A, respectively, being significantly lower than the top panel current.

Figure 16 shows that replacement of the electron VTF current to the ion VTF current begins around Z=285 mm and almost completes around Z=294 mm, that is, just before the ion dominant sheath. The simulated ion current profile on the top panel is essentially coincident with the current profile onto the top electrode array as shown

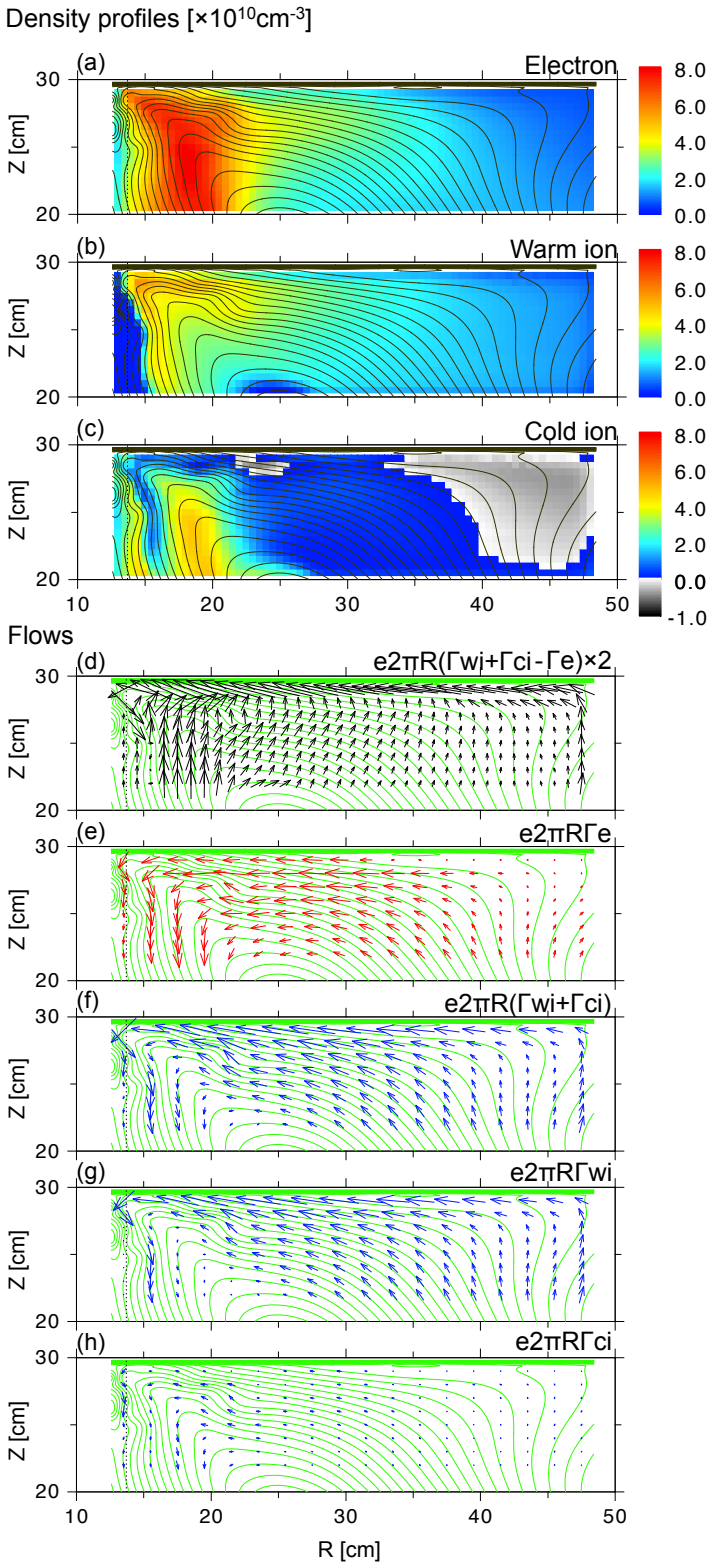

Figure 15. Simulation results for ion enhanced drift toward the top panel driven by the cross field potential hill. (a) electron density profile replotted from figure 9(a), (b) and (c) density profiles of warm and cold ions, respectively, flow patterns of (d) electric current, (e) electrons, (f) ions, (g) warm ions and (h) cold ions. Analyses for the 1.9 kW hydrogen plasma.

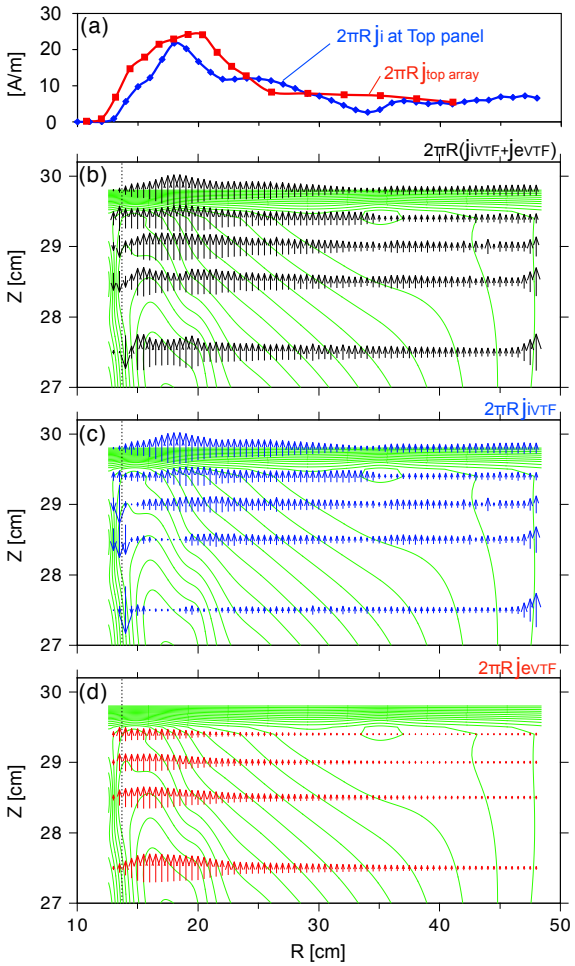

Figure 16. (a) Experimental current profile onto the top electrode array (red line) and modeled current profile onto the top panel (blue line). (b)-(d) Developments of $j_{eVTF} + j_{iVTF}$, j_{iVTF}, j_{eVTF}. All the current densities are weighted by $2\pi R$. Here, j_{iVTF} is defined as $j_{iVTF} = e(\Gamma_{i\_Z} - \Gamma_{E\times B\_Z})$. Analyses for the 1.9 kW hydrogen plasma.

in top box in the figure.

3.6. Ion dominant sheath

The space potential is still as high as $\approx$ 15 V in the very vicinity of (3.5 mm apart from) the top panel as shown in figure 17(b). This result implies that the excess portion of singly ionized ion density over the electron density in this thin layer on the top panel is higher than $\sim 10^8 cm^{-3}$, which is much higher than the excess at the potential hill $\sim 10^5 cm^{-3}$. Thus an ion dominant sheath develops on the top panel surface. The detailed potential profile toward the panel is, however, unknown. For reference we apply the Child-Langmuir model using $j_{top\ array}$ and V_S in figure 17 (a) and (b) as the Voltage and the current density for the Child-Langmuir formula [24], respectively, to estimate

the sheath width shown in figure 17(c). An example of full Child-Langmuir result at R=18 cm is shown in figure 18(a).

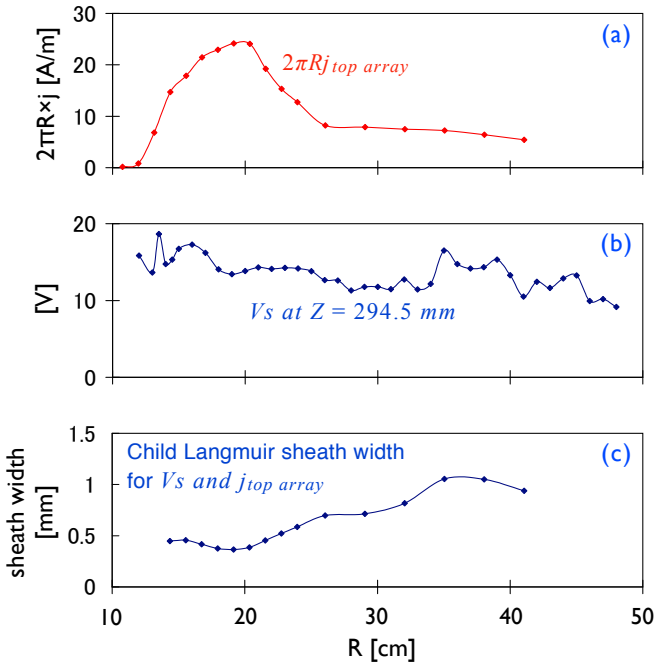

Figure 17. (a) Current density onto the top electrode array, (b) space potential in front of the top panel and (c) Child-Langmuir sheath width using the data in (a) and (b). Analyses for the 1.9 kW hydrogen plasma.

Electrons having moderate kinetic energy, say ∼5 eV, would climb up the very steep sheath potential (see figure 13) and leave the sheath. Therefore the electrons in the sheath would be cold and completely magnetized while they have a large $E \times B$ drift velocity toward the ECR layer. These cold electrons may be supplied from the area around the vessel side wall near the periphery of the top panel.

A case for the sheath width of 2 mm is shown in figure 18(b) which is easily obtained based on the result shown in figure 18(a). The excess potion of ion density in this case is 4% of the electron density. Note that this result is, however, not quite the case since the electron density just before the panel surface must be zero, at least in the range of electron Larmor radius from the surface, ∼0.1 mm.

3.7. Enhanced electron VTF drift onto the bottom panel

The electron density profile near the bottom panel in the 1.2 kW argon plasma reflects large ion Larmor radius of argon ion Ar^+ as shown in figure 19. Even if kinetic energy of Ar^+ is as low as 0.1 eV its Larmor radius is as long as 5 mm at R=22 cm. The ion density must be the same as the electron density near the bottom panel since there is no potential gap onto the bottom panel surface. The electron flux down onto the bottom panel should be constant along the vertical chord onto the panel. Here the electron

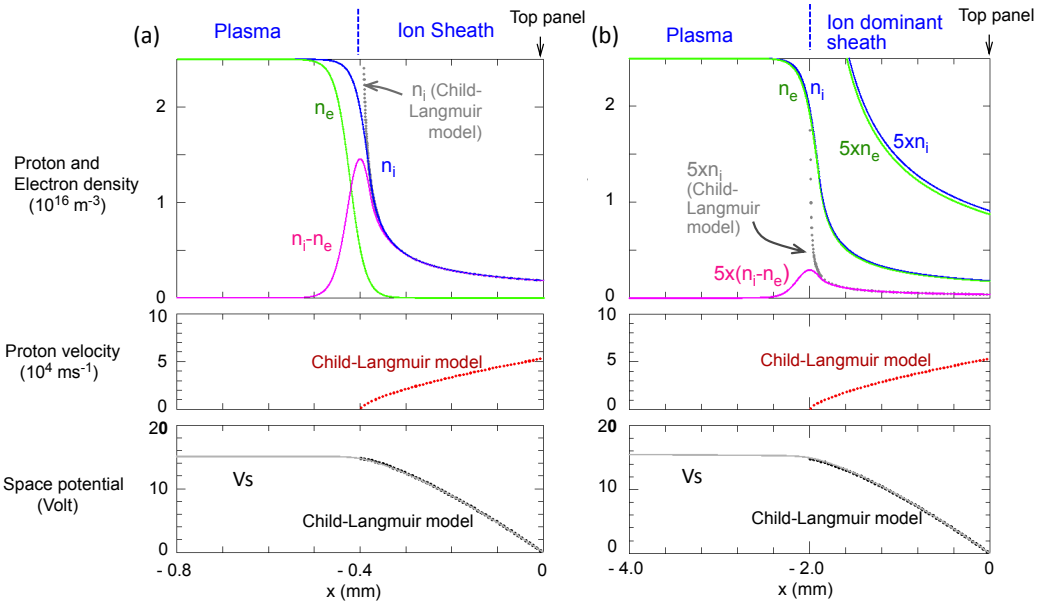

Figure 18. (a) Electron and ion density profiles matched to the Child-Langmuir model. (b) Electron and ion density profiles to model ion dominant sheath having a sheath width of 2mm, being much wider than the Child-Langmuir case of 0.4 mm. Sheath voltage = 15 Volt and sheath current density=20 Am^{-2} in both (a) and (b).

VTF drift velocity is much faster than the $E \times B$ drift velocity as estimated from figure 19. Therefore the flux is approximately proportional to the electron pressure. Figure 19 shows, however, that while the electron temperature increases toward the panel, the increment is not large enough to compensate the decrement of the density and the electron pressure also decreases toward the panel. Similar tendency is seen on the electron density and temperature profiles of the hydrogen plasmas in figure 5. This is one of questions which are not resolved in the present experiment.

A possible explanation is that the electrons are heated strongly to the perpendicular direction when they VTF drift down the density slope toward the panel. This perpendicular heating may be hardly detected on the V-I characteristics of Langmuir probe as explained previously in section 3.2. In addition, the narrow empty gap between the panel and the plasma which arises due to the steep and pointed density down slope around R=22 cm might focus and intensify the wave field to heat the electrons so strong that the electron flux becomes constant.

3.8. Seed electrons for impact ionization

There is an electron $E \times B$ flow across the ECR layer from low field side between the potential hill and the top panel as shown in figure 20(a). In addition there would be a flow of electrons in the sheath by fast $E \times B$ drift ($V_{E\times B} \sim 10^5 ms^{-1}$) across the ECR layer. These electrons may flow down along the equipotential contours, again across the ECR layer from the high field side and work as seed electrons for impact ionization to

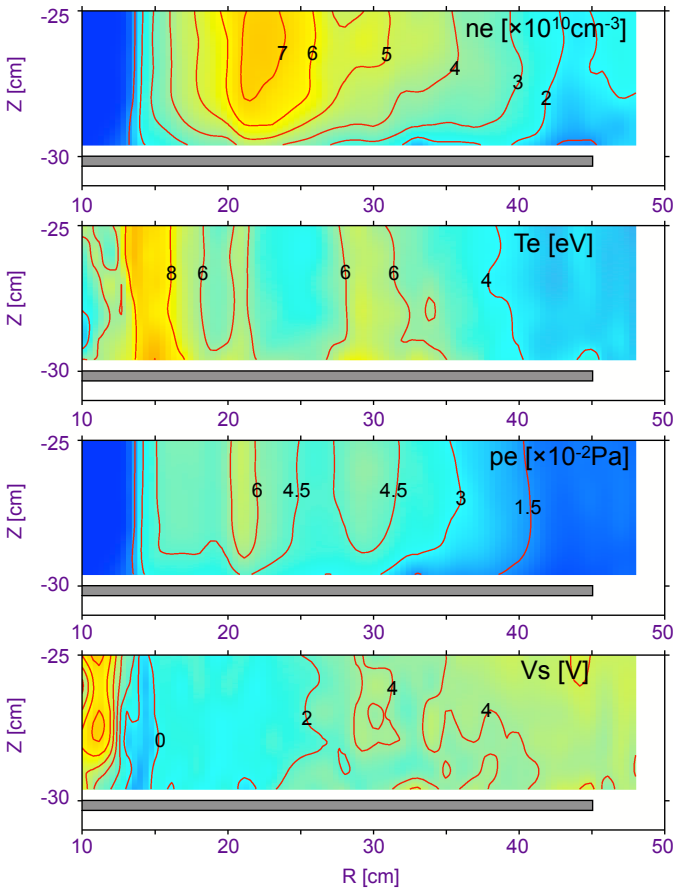

Figure 19. Detailed profiles of electron density, temperature, pressure and space potential near the bottom panel in the argon 1.2 kW plasma in figure 5. Note that the figures are vertically stretched.

maintain the discharge. The electron temperature profile shown in figure 20(c) shows that EC heating is already strong at just higher field side of the ECR layer. Some seed electrons may be quickly heated to the energy range high enough to ionize hydrogen molecule as shown in figure 20(d), and the density quickly increase toward the lower field side as shown in figure 20(b).

Percentage of the seed electron flux are estimated to be $2 \sim 4\%$ of the electron flux out to the boundary for the hydrogen and argon discharge plasmas shown in figure 5. These electrons may serve as a stabilizer of the discharge. In another experiment toroidal filed has been slowly decreased so that the ECR layer moves to and hidden into the center post during 2.5 second microwave injection. Once the ECR layer moves into the center post the discharge terminates, again suggesting importance of seed electrons provided from the high field side toward the ECR layer for discharge maintenance.

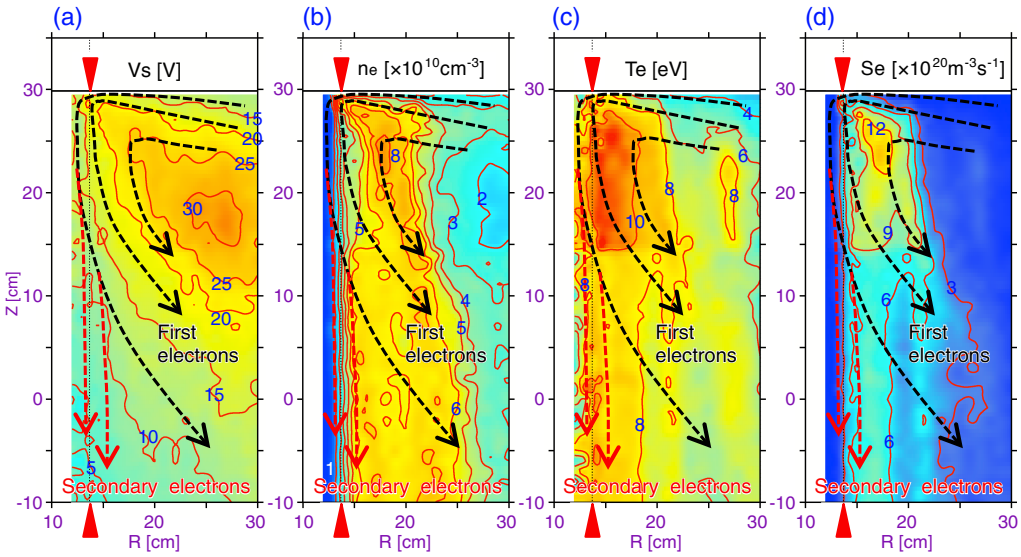

Figure 20. Electron circulation around the potential hill and across the ECR layer provides seed electrons to the ionization belt from higher field side. Red triangles show the location of the ECR layer. Analyses for the 1.9 kW hydrogen plasma.

4. Discussions

4.1. Effect from non-axis-symmetricity of boundary

Most subtle point of the experiments is the effect of non-flatness of the bottom panel. There is a deviation of ∼1 mm from the flatness as described in section 2. This length is much shorter than the ion Larmor radius but much longer than the electron Larmor radius. The radial potential profile from the Langmuir probe measurement at the nearest location to (4 mm apart from) the bottom panel still shows the same magnitude of vertical $E \times B$ drift as the $E \times B$ drift on the Z=−290 mm plane (10 mm from the panel) in the range of R=18-32 cm. In figure 10 both ion and electron $E \times B$ flux onto the bottom panel is estimated to be ∼1 A. While the estimation for ion flux onto the bottom panel seems reasonable since this is the range of the ion Larmor radius, the estimation for electrons lacks confidence from the point of Larmor radius since equipotential contour must be parallel to the panel surface in the very vicinity of the surface. One possibility is that the electrons first $E \times B$ drift down into the shadow of the panel undulation and then flow into the panel surface along the field lines.

Second non symmetric point is the presence of radial port holes on the side wall of the vessel (see figure 2). If the side wall is completely cylindrical, the electron flux to the side wall may be much smaller than the ion flux again due to the difference in the Larmor radii. Once the plasma flows into the hole by the $E \times B$ drift along the equipotential contours, the electrons easily flow into the vessel along the field lines. The results in figure 10 suggest that while most of the ion and electron fluxes across the cylindrical surface of R=48 cm flow into the vessel, a small portion of electron flux

may leave the area along the vessel wall and flow toward higher field side along the ion dominant sheath in front of the top panel.

Usual devices have many non-symmetric obstacles in the vessel that face the plasma. An interesting question is whether or not the picture on the electron and ion flows for the present experiment, in particular replacement of carrier of charge separation current from electrons to ions near the ion drift side wall, are still the case in ECR plasmas in these devices ? Previous experiments in the LATE device nearly the same eccentric potential hill was generated and also similar vertically stretched uniform pressure ridge was formed along the ECR layer in spite of the presence of large local limiters on the top and bottom panels that violate the symmetry. This result suggests that the picture may also be the case in these devices as well.

4.2. Effect of finite ion Larmor radius

The $E \times B$ drift velocity is the same for the electrons and ions, and the drift does not generate any electric current if their Larmor radii are much shorter than the scale length around their guiding centers. This criterion is obviously violated at the boundary. The difference in Larmor radii between electrons and ions gives rise to the ion dominant sheath on the top panel and also some distortion on density and pressure profiles on the area of steep potential slope near the potential peak as well. Except for these regions the $E \times B$ drift does not generate appreciable current in the main plasma, where vertically uniform ridge of electron pressure arises as predicted by equation (5). Note that the ion temperature is much lower than the electron temperature near the pressure ridge. The prediction, however, does not quite hold at the high field side of the potential hill, where the potential slope is steep as mentioned above. In particular deviation from the prediction is most significant in the argon plasma.

4.3. Discharge maintenance

The vertically uniform ridge on electron pressure profile indicate that electron production via electron impact ionization and subsequent ECR-driven VTF drift of these electrons to downward is the primal engine that drives the plasma. The driven electrons leave the ions behind. The experimental observations show that this inherent charge separation does not terminate the discharge; instead, it generates the cross field potential hill of moderate magnitude in the upper side. The hill, then, regulate the electron and ion flows from the source to the boundary. In particular, the ion enhanced VTF-drift flow toward the top panel and the electron VTF-drift flow down to the bottom panel are the main flows to keep the plasma charge neutrality very high. As the injection power increases, the additional $E \times B$ flow toward the side vessel wall increases.

Now let us ask what happens when the ion flow to the top panel deteriorates transiently? Even if the deterioration is quite a trifle, the potential would quickly rise and the ion enhanced VTF-drift flow to the top panel would increase. Then the balance between the electron and ion flows to the boundary would recover and also the potential

would recover to the original equilibrium level as well. Excessive accumulation of positive charge in the plasma would be avoided. In the opposite case similar feedback may work as well. Thus the present picture of the ion enhanced VTF-drift flow to the top panel driven by the cross field potential hill can macroscopically keep the electron and ion flows steady.

It is, however, still not understood how the charge neutrality is kept so high as 10^{-5} everywhere in the main plasma in spite of the inherent charge separation drifts between the electrons and ions everywhere in the main plasma. Processes in ECR plasmas are full of variety, quite complicated and subject to many uncontrollable disturbances; ion species, various ionizations and dissociations, impurities, boundary conditions including various diagnostic electrodes, microwave powers and absorptions, etc. It is surprising that the high charge neutrality always holds everywhere in the main plasma under variety of these complicated factors.

5. Summary

In electron cyclotron resonance (ECR) plasmas immersed in the toroidal field, the electrons drift downward while the ions drift upward due to the field gradient and curvature. Many experiments in past decades showed that the ECR plasma was easily initiated and maintained by the microwave power. This result indicates that steady flows of electrons and ions from the source to the surrounding conducting walls are always realized under the inherent charge separation drifts between electrons and ions.

In order to find in what way the electrons and ions flow steadily and stably to the boundary we have done experiments in the low aspect ratio torus experiment (LATE) device using a 2.45 GHz microwave power around 1 kW. We have set the top and bottom panels in the cylindrical vessel, where those panels and the vessel wall constitute the conducting boundary, and fabricated electrode arrays, an ion energy analyzer and Langmuir probes for diagnostics.

We have found that a vertically uniform ridge of electron pressure that also constitutes the source belt of electron impact ionization is formed along just lower field side of the ECR layer and a cross-field potential hill ($V_S \cong$30 V while $T_e \cong$10 eV), eccentrically shifted toward the corner formed by two lines of the top panel and the ECR layer, arises in the upper part of the plasma.

Combination of electron production via electron impact ionization and subsequent ECR-driven VTF drift of these electrons to downward along the pressure ridge is the primal engine that drives the plasma. The driven electrons leave the ions behind. This inherent charge separation does not terminate the discharge; instead, it generates the cross field potential hill of moderate magnitude which regulates the electron and ion flows as follows.

The hill adds $E \times B$ drift to the VTF drift to adjust the flows of electrons and ions to keep charge neutrality in a high level of $\sim 10^{-5}$. In particular, the ions, of which VTF drift velocity is much slower than the electron VTF drift velocity near the source belt,

are carried by the $E \times B$ drift around the hill to the vicinity of the top panel, where the ion VTF drift increases strongly on the steep down slope of potential toward the top panel. On the other hand the electron temperature strongly decreases in this area. Thus the carrier of VTF drift current is replaced from the electrons to the ions before the top panel, enabling the current circulation through the top and bottom panels and the vessel (electrons mainly to the bottom and ions mainly to the top). This may keep charge neutrality very high and electric field moderate. A few percent of electrons from the source turn around the hill by 360 degree and reentry the source belt from the high field side as seed electrons for the impact ionization, keeping the discharge stable.

6. Acknowledgment

The present work was supported by JSPS KAKENHI (Grant Number 23360411 and 26289357) and NIFS collaboration program in Japan. Information on various aspects of electron impact ionization and dissociation of hydrogen molecule from Professors Sawada and Fujimoto was quite useful.

References

[1] Peng Y-K M, Borowski S K and Kammash T 1978 Nucl. Fusion 18 1489
[2] Nakao S, Ogura K, Terumichi Y and Tanaka S 1983 Phys. Lett. A 96 405
[3] Gilgenbach R M et al 1981 Nucl. Fusion 21 319
[4] Kubo S, Nakamura M, Cho T, Nakao S, Shimozuma T, Ando A, Ogura K, Maekawa T, Terumichi Y and Tanaka S 1983 Phys. Rev. Lett. 50 1994
[5] Toi K et al 1984 Phys. Rev. Lett. 52 2144
[6] Parail V V, Pereverzev G V and Vojtsekhovich I A 1985 Proc. 10th Int. Conf. on Plasma Physics and Controlled Nuclear Fusion (London, 1984) vol 1, p 605, IAEA-CN-44/F-IV-4 (Vienna: IAEA)
[7] Zakharov L E and Pereverzev G V 1988 Sov. J. Plasma Phys. 14 75
[8] Müller S H, Fasoli A, Labit B, McGrath M, Podestá M, and Poli F M 2004 Phys. Rev. Lett. 93 165003
[9] Podestá M, Fasoli A, Labit B, McGrath M, Müller S H and Poli FM 2006 Plasma Phys. Control. Fusion 48 1053
[10] Furno I et al 2008 Phys. Rev. Lett. 100 055004
[11] Perez J C, Horton W, Gentle K, Rowan W L, Lee K and Dahlburg R B 2006 Phys. Plasmas 13 032101
[12] Rypdal K, Grønvoll E, Ømynes F, Fredriksen Å, Armstrong R J, Trulsen J and Pétcseli H L 1994 Plasma Phys. Control. Fusion 36 1099
[13] Forest C B, Hwang Y S, Ono M, and Darrow D 1992 Phys. Rev. Lett. 68, 3559
[14] Forest C B et al. 1994 Phys. Plasmas 1 1568
[15] Maekawa T et al 2005 Nucl. Fusion 45 1439
[16] Yoshinaga T, Uchida M, Tanaka H, and Maekawa T 2006 Phys. Rev. Letters 96 125005.
[17] Yoshikawa S, Harries W I and Sinclair R M 1963 Phys. Fluids 6 1506
[18] Nishi S, Sakabe T, Uchida M, Tanaka H and Maekawa T, 2010 Plasma Phys. Control. Fusion 52 065011
[19] Nishi S, Sakabe T, Uchida M, Tanaka H and Maekawa T, 2010 Plasma Phys. Control. Fusion 52 125004

[20] Stangeby P C, *The Plasma Boundary of Magnetic Fusion Devices*, (Taylor and Francis, New York and London, 2000)(see figure 1.25)
[21] Sawada K and Fujimoto T, 1995 J. Appl. Phys. 72, 2913.
[22] Peart B and Dolder K T,1971 J. Phys. B: Atom. Molec. Phys. 4 1497
[23] Kengoh K, Uchida M, Tanaka H, and Maekawa T 2012 Plasma and Fusion Research 7 1302098
[24] Goldston R J and Rutherford P H, *Introduction to Plasma Physics*, (Institute of Physics Publishing, Bristol and Philadelphia, 1995)(see Section 1.4)